Supplementary information

Determination of excitation energy transfer efficiency in individual artificial light-harvesting complexes mimicking chlorosomes

Tomas Malina[1], Ashley M. Hancock[2,3,$], Sophie A. Meredith[2,3], Peter Kapusta[4], David Kaftan[5], Peter G. Adams[2,3], Jakub Psencik[1]

[1]Department of Chemical Physics and Optics, Faculty of Mathematics and Physics, Charles University, Prague 121 16, Czech Republic

[2]School of Physics and Astronomy, University of Leeds, Leeds LS2 9JT, United Kingdom

[3]Astbury Centre for Structural Molecular Biology, University of Leeds, Leeds LS2 9JT, United Kingdom

[4]J. Heyrovský Institute of Physical Chemistry, Czech Academy of Sciences, Prague 182 23, Czech Republic

[5]Czech Academy of Sciences, Institute of Microbiology, Centre Algatech, Novohradská 237, 37981 Třeboň, Czech Republic

[$] Current address: ICFO-Institut de Ciencies Fotoniques, The Barcelona Institute of Science and Technology, Castelldefels, Barcelona 08860, Spain

Contents

1 Derivation of efficiency of EET

In single-particle measurements, typically only a small number of photons are detected for each particle. This makes proper spectral analysis challenging. It is therefore sensible to use band-pass filters instead and measure signals in their spectral channels. While for bulk samples the efficiency of EET can be determined by comparing the areas or amplitudes of donor and acceptor contributions in measured spectra, this is no longer possible if fluorescence is integrated in spectral channels. Despite this, the equation for efficiency of EET can still be derived exactly as long as the shape of the donor emission spectrum doesn't change when an acceptor is added. From our previous experiments on bulk samples, we know that this is true for BChl aggregates [1, 2]. Therefore, steady-state bulk spectra are used to determine the donor and acceptor contributions in each of the spectral channels, as illustrated below (Fig. S1 below, Fig. 2 in the main text). The signal intensity measured in each spectral channel then consists of the contribution from both pigments.

(S1)
$$
\begin{aligned}
{}^{\mathrm{D+A}}I_{840} &= {}^{\mathrm{D+A}}F^{\mathrm{A}}_{840} + {}^{\mathrm{D+A}}F^{\mathrm{D}}_{840} = {}^{\mathrm{D+A}}F^{\mathrm{A}} \cdot \mathrm{r}^{\mathrm{A}}_{840} + {}^{\mathrm{D+A}}F^{\mathrm{D}} \cdot \mathrm{r}^{\mathrm{D}}_{840} \\
{}^{\mathrm{D+A}}I_{750} &= {}^{\mathrm{D+A}}F^{\mathrm{A}}_{750} + {}^{\mathrm{D+A}}F^{\mathrm{D}}_{750} = {}^{\mathrm{D+A}}F^{\mathrm{A}} \cdot \mathrm{r}^{\mathrm{A}}_{750} + {}^{\mathrm{D+A}}F^{\mathrm{D}} \cdot \mathrm{r}^{\mathrm{D}}_{750}
\end{aligned}
$$

Where following notation is used ${}^{\mathrm{Sample}}x^{\mathrm{pigment}}_{\mathrm{channel}}$, with D and A denoting donor and acceptor, *I* denotes the detected signal intensity, *F* denotes fluorescence emission intensity of the specific component (pigment), and r the fraction of fluorescence emitted from the given pigment in the selected spectral channel. These ratios r can be obtained from steady-state spectra of the bulk samples, which were fitted by two curves representing the contributions of the acceptor and donor, with areas ${}^{\mathrm{D+A}}F^{\mathrm{A}}$ and ${}^{\mathrm{D+A}}F^{\mathrm{D}}$ (Fig. S1). Then r is defined as the area under one of the curves (representing A or D) within one spectral channel (750 or 840 nm) divided by the total measured fluorescence of this component, ${}^{\mathrm{D+A}}F^{\mathrm{A}}$ or ${}^{\mathrm{D+A}}F^{\mathrm{D}}$, respectively (Table S1). The areas were determined when plotted in energy units (not in wavelengths, as displayed here) and the obtained values are shown in Table S1.

Table S1: calculated fractions r used for calculations of single-particle efficiency of EET.

Sample BChl *c*:β-carotene:BChl *a* ratio	$\mathrm{r}^{\mathrm{D}}_{750}$	$\mathrm{r}^{\mathrm{D}}_{840}$	$\mathrm{r}^{\mathrm{A}}_{750}$	$\mathrm{r}^{\mathrm{A}}_{840}$
1:0.0:0.25	0.528	0.104	0.003	0.697
1:0.1:0.25	0.541	0.106	0.004	0.712
1:0.3:0.25	0.539	0.109	0.004	0.708
1:0.5:0.25	0.548	0.105	0.005	0.713

The values were determined for every sample separately, because it was previously found that the emission spectra change slightly depending on carotenoid content [2]. Similarly, the calculated ratios change slightly with carotenoid content.

The fluorescence intensity detected in each of the spectral channel consist of contributions from both acceptor and donor (filled areas in Fig. S1). The contributions/ratios are visualized as the solid area vs the striped area (Fig. S1).

To determine the efficiency of energy transfer, the ratio of fluorescence intensity emitted from the acceptor (Fig. S2: magenta area) to the decrease of fluorescence intensity from the donor after the addition of the acceptor (Fig. S2: blue area) is needed and is later for simplicity called partial quantum efficiency, QE. This would be the actual fluorescence quantum yield of the acceptor if the spectra were measured across all wavelengths. However, our detection range was limited, so we could not measure the full spectra, and therefore this value is not the actual quantum yield but is closely related. These ratios are 0.307, 0.343, 0.375, and 0.498 for samples with beta-carotene concentrations of 0, 1.5, 4.5, and 7.5 µM):

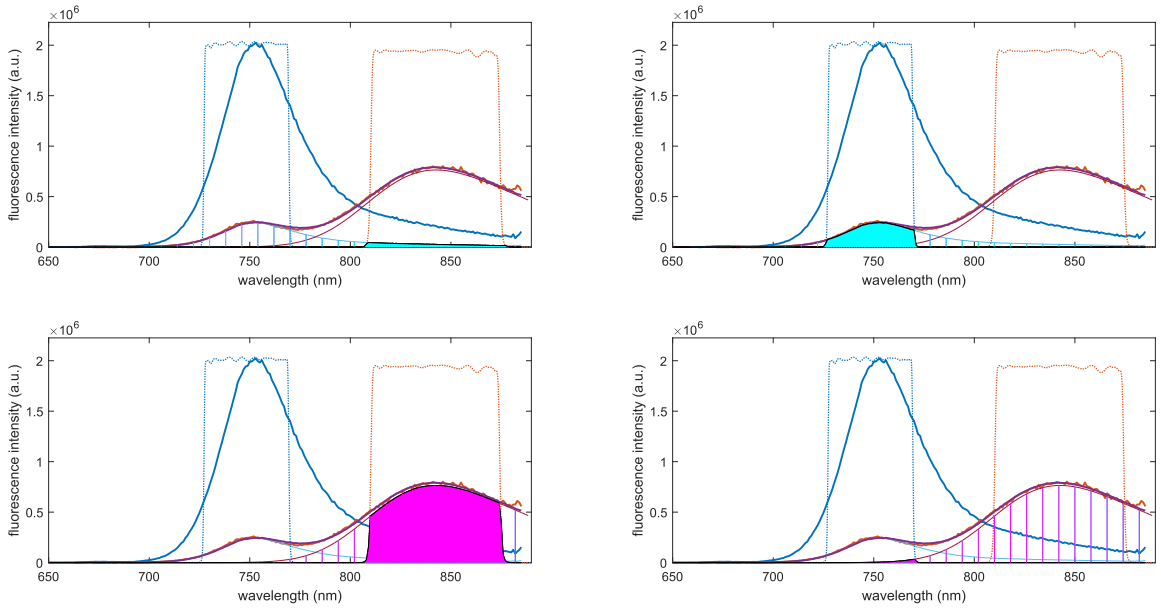

Figure S1: Left to right top row r_{840}^{c} and r_{750}^{c}, left to right bottom row r_{840}^{a} and r_{750}^{a} are calculated as the ratios of the solid vs striped areas. All plots show the steady-state fluorescence emission spectra of BChl aggregates without BChl *a* (blue curve) and with BChl a as acceptor (orange curve). The orange curve is than decomposed into components of BChl *c* contribution (thin cyan curve) and BChl *a* contribution (thin magenta curve). The plots are displayed in wavelengths on the x axis, but the areas are calculated in energy units.

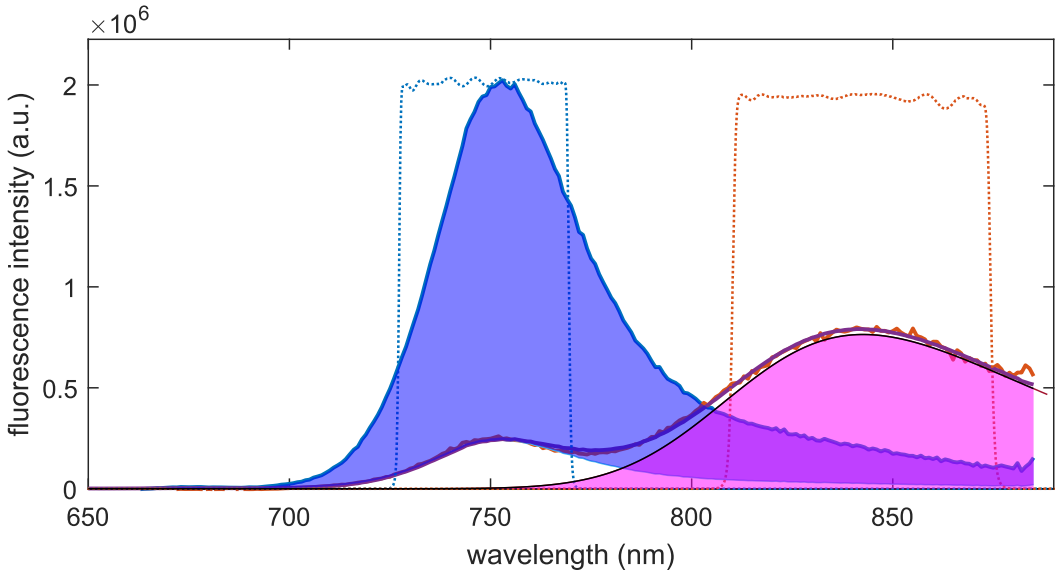

Figure S2: Illustration of the calculated partial quantum efficiency related to the quantum yield of fluorescence. This ratio is sufficient for the calculations: as long as the range of all measured spectra is kept constant and the same range of wavelengths is used to calculate the fractions r, it will still provide exact results without approximations.
Note: the plot is displayed in wavelengths on the x axis, but the areas are calculated in energy units. This can be visually misleading as the magenta area appears much larger.

In our case, the donor pigment is BChl *c* and the acceptor is BChl *a*. Solving for the total fluorescence ${}^{c+a}F^{a}$ and ${}^{c+a}F^{c}$ in terms of the recorded fluorescence intensities in respective spectral channels, we get (rewritten Eq. S1):

$$
\begin{aligned}
{}^{c+a}I_{840} &= {}^{c+a}F^{a} \cdot r^{a}_{840} + {}^{c+a}F^{c} \cdot r^{c}_{840} \\
{}^{c+a}I_{750} &= {}^{c+a}F^{a} \cdot r^{a}_{750} + {}^{c+a}F^{c} \cdot r^{c}_{750} \\
{}^{c+a}F^{c} &= \frac{{}^{c+a}I_{750} \cdot \mathrm{r}^{a}_{840} - {}^{c+a}I_{840} \cdot \mathrm{r}^{a}_{750}}{\mathrm{r}^{c}_{750} \cdot \mathrm{r}^{a}_{840} - \mathrm{r}^{c}_{840} \cdot \mathrm{r}^{a}_{750}} \\
{}^{c+a}F^{a} &= \frac{{}^{c+a}I_{840} \cdot \mathrm{r}^{c}_{750} - {}^{c+a}I_{750} \cdot \mathrm{r}^{c}_{840}}{\mathrm{r}^{c}_{750} \cdot \mathrm{r}^{a}_{840} - \mathrm{r}^{c}_{840} \cdot \mathrm{r}^{a}_{750}}
\end{aligned}
\qquad \text{(S2)}
$$

As established above, the blue area in Fig. S2 can be expressed in terms of the magenta area and the partial radiative quantum efficiency (QE_a, Eq. S3). Then, the efficiency of energy transfer from BChl *c* to BChl *a* can be determined as the decrease of BChl *c* fluorescence after adding BChl *a* (the blue area in Fig. S2 vs the whole area under the same curve, Eq. S4). This way, we obtain the efficiency of EET independent of the fluorescence of donor-only samples, allowing us to determine the efficiency of EET in real time for individual particles.

Using the introduced definition for QE_a

(S3) $$\mathrm{QE}_a = \frac{{}^{c+a}F^a}{{}^{c}F^c - {}^{c+a}F^c}$$

we obtain

(S4) $$EET = \frac{{}^{c}F^c - {}^{c+a}F^c}{{}^{c}F^c} = \frac{\frac{{}^{c+a}F^a}{\mathrm{QE}_a}}{\frac{{}^{c+a}F^a}{\mathrm{QE}_a} + {}^{c+a}F^c} = \frac{{}^{c+a}F^a}{{}^{c+a}F^a + \mathrm{QE}_a\,{}^{c+a}F^c}$$

Substituting for total fluorescence intensities in terms of measured channel intensities (Eq. S2):

(S5) $$EET = \frac{{}^{c+a}I_{840}\cdot \mathrm{r}_{750}^{c} - {}^{c+a}I_{750}\cdot \mathrm{r}_{840}^{c}}{{}^{c+a}I_{840}\cdot \mathrm{r}_{750}^{c} - {}^{c+a}I_{750}\cdot \mathrm{r}_{840}^{c} + \mathrm{QE}_a\left({}^{c+a}I_{750}\cdot \mathrm{r}_{840}^{a} - {}^{c+a}I_{840}\cdot \mathrm{r}_{750}^{a}\right)}$$

The intensities *I* in this formula are the true emitted signal intensities. Due to artifacts, recorded signals need to be corrected for noise/background and setup sensitivity to obtain these true signal intensities. The processes of correction and calibration is described in later chapters.

2 Background subtraction – detailed description

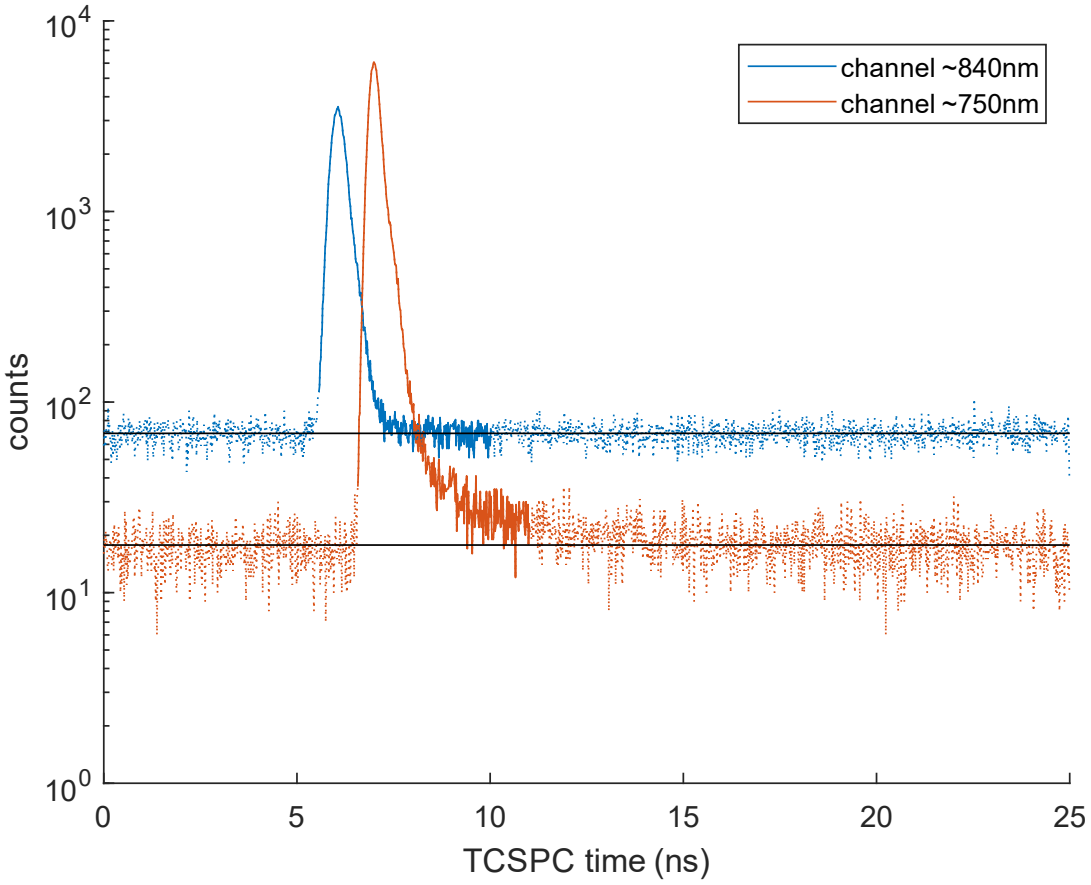

Figure S3: histograms of detected photon arrival times for one of the measurements of floating samples.

Background was present on both SPAD detectors used to measure floating samples to a different extent; therefore, it was necessary to subtract background for each detection channel separately. We measured time-tagged time-resolved data, and thus we were able to make a histogram of all photon arrival times (Fig. S3). By keeping only photons that arrived during and right after the excitation pulse and excluding other arrival times, we removed most of the background in both detection channels (photons shown by dotted lines were excluded from analysis). The number of signal bins for both channels was kept the same even though the signal appeared to decay faster in the 840-nm channel – this is only because of the worse signal-to-noise ratio; in fact, the FWHM of the curve in the 840-nm channel is approximately one third larger than in the 750-nm channel (442 vs 332 ps, see M&M in the main text). However, background (mostly detector after-pulsing and dark counts - the mean background level is visualized by black horizontal lines in Fig. S3) can be detected at any time, so it was necessary to also compensate for the background in the selected (time-gated) part (Fig. S3 solid lines) of the histogram. Therefore, an average value of background signal per bin per unit of time was calculated – here, for the 840-nm curve, the background

signal was 68.5 photons per bin over the whole 10-minute measurement on average. This corresponds to a contribution of approximately 0.1 photon per bin per second. The time-gated signal window was 280 bins long (~4.5 ns), thus the background in this channel (for all highlighted arrival times) was 31.98 counts per second (cps) on average. For the 750-nm detection channel, this background is only 8.96 cps.

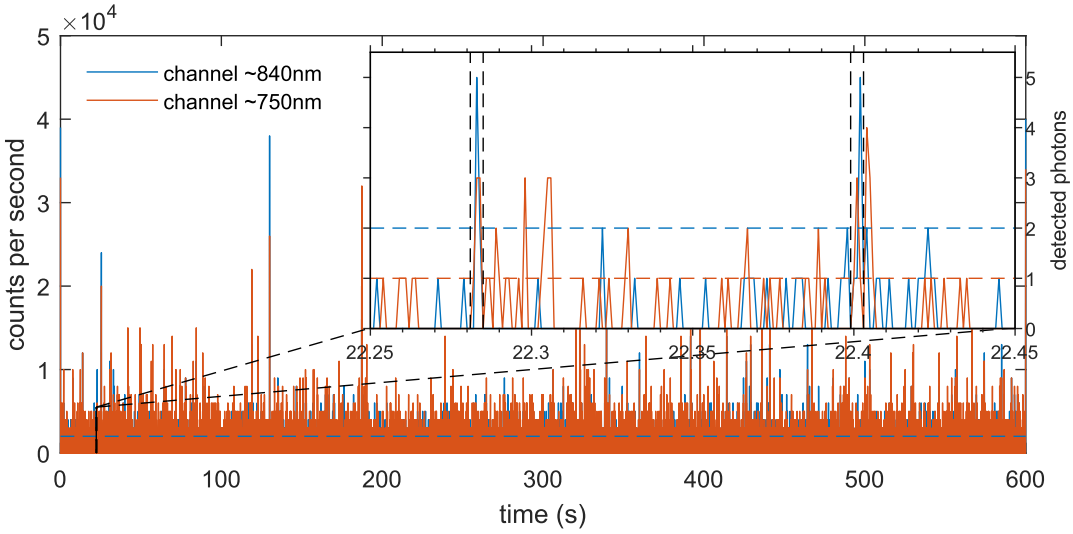

Figure S4: time-trace of one illustrative measurement with detected particles highlighted by vertical dashed lines and detection threshold indicated by horizontal dashed lines. Peaks that surpass the detection threshold in both channels are selected and the photons accumulated between the vertical lines are used for calculation. The signal is not yet corrected for channel sensitivity (see the following section) but is corrected for background.

In the time-trace signal for floating-particle samples (Fig. S4), we already show only photons that were detected during the time-gated arrival times (solid line in Fig. S4), but the calculated counts-per-second (CPS) background is still present. When we detect particles as highlighted by the black dashed vertical lines, we need to measure the particle residence time in the focal volume and subtract the appropriate background from the detected signal, which is the maximum likelihood estimation for the signal. The first highlighted particle stays in the focal volume for 4 ms, therefore from all the photons detected in the blue and orange channel for this particle, we need to subtract 0.004*31.98 and 0.004*8.96, or 0.13 and 0.04 counts. Therefore, the fluorescence intensities detected for this particle in the orange and blue channels are not 7 and 7 counts, but 6.87 and 6.96 counts, respectively, when background is subtracted. By cross-referencing detections found in both channels, we avoid a statistical bias of only selecting exclusively the brightest BChl *c* or brightest BChl *a* particles, which would skew the calculated efficiencies towards the lowest and highest efficiencies of EET present in the sample, respectively.

Since photons are detected randomly, it is technically possible that if we detect a particle in one detection channel, the other detection channel can have fewer counts over the same

period of time than what would correspond to background. In such a case, subtracting background would make the intensity negative, and the later calculated efficiency of EET would be unphysical. These particles would therefore need to be excluded from analysis. However, we have encountered no such case.

In immobilized samples, the time-gating of relevant photon arrival times was used similarly (as shown in Fig. S3 for liquid samples). Furthermore, a fixed threshold of 2 photons per pixel was enforced, removing all pixels with 1 and 2 detected photons. This ensured random single-photon detections were not counted, while it kept the number of removed photons to a minimum. Lastly, any singular bright pixels encompassed by 8 totally dark pixels were removed, too, as they were deemed unreliable detections. The pixel size was ~100 nm, which is below the diffraction limit, therefore any real particle should cover multiple adjacent pixels. The procedure is visualized in *Section 8*.

Similarly to the floating-particle samples, only a small amount of detection events was excluded from analysis this way, and if any real particles were eliminated this way, those particles had the highest shot noise.

3 Detection event filtering

The standard approach is to use a statistical test to select a false positive detection rate. The background of photon-counting detection is Poisson-distributed (the variance equals the mean). Therefore, the threshold at which there is a 1% probability of mistaking background for a particle (parameter alpha = 0.01) is determined as the 99th percentile of the cumulative distribution function for the corresponding background level. This average background level was determined with time-gating for each channel in the previous section (black lines in Fig. S3 in *SI, Section 2*).

To find out whether all types of particles – large and small, bright and dim – are detected in our floating samples by this approach, the analysis of efficiencies of EET with different arbitrary detection thresholds was performed – approximately 1%, 5%, 25% and 50% brightest detection events with 2 or more photons in each detection channel were selected for analysis[1] and then cross-referenced between channels for co-localized detection. The sensitivity correction was kept the same in this case, calculated from the Poisson threshold detections, in order to compare if there is a change in the efficiencies calculated from particles of different brightness levels – this way, the intensity-weighted mean efficiencies obtained from the single particles were no longer normalized to the bulk results for each threshold. The table below (Table S2) lists the average efficiencies of all particles detected using these arbitrary thresholds, clearly showing that the efficiency of EET in particles with vastly different brightness levels within one sample does not change.

Therefore, selecting a different threshold does not noticeably affect the calculated efficiencies in our case, and we can select the parameter alpha for false positive detection virtually arbitrarily. We kept the parameter at 1% to include a large number of detected particles while keeping the false positive rate (type I error) low.

Table S2: mean efficiencies of EET (in %) for four samples containing 15 µM BChl *c*, 3.75 µM BChl *a* and different concentrations of β-carotene determined for particles of different brightness levels.

% of brightest detections included	Efficiency of energy transfer (%) for samples with concentration of beta-carotene: 0 µM	1.5 µM	4.5 µM	7.5 µM
1	93.5	93.5	88.1	86.0
5	93.5	92.9	89.1	85.8
25	93.4	93.3	88.3	86.5
50	93.4	93.3	90.0	86.1

From the histograms (Figures S5–8) one can see that the distribution initially gets smoother as more particles get included. However, particularly in Fig. S7 and S8, this stops being the

[1] These percentage thresholds are not exact percentages of included particles, they are the maximum fractions of brightest detection events allowed to be included in the analysis. Due to low signal (high shot noise), the actual percentages of included particles were lower – see the end of this section for details.

case. The prominent spikes in the histograms are caused by shot noise – the low discrete photon counts detected for each dim particle are the cause. For those dim detection events, only a handful of photons are detected, and adding or missing one photon will shift the calculated efficiency over several bins – therefore, only some of the histogram bins get a contribution from these dim particles, which are the spikes in the distribution. This artifact is less slightly pronounced in low-carotenoid samples due to the narrower distribution but is still visible for the 75th and 50th percentile threshold.

Lowering the threshold further did not have any effect on the histogram as there were no additional particles added – at 50% threshold of all detections, all detection events with 2 or more photons in both detection channels were already included (for samples with the lowest two carotenoid concentrations, this is already the case at 25% of brightest particles). Including 1-photon high peaks would mean there is no detection threshold, and 100% detections are taken into account.

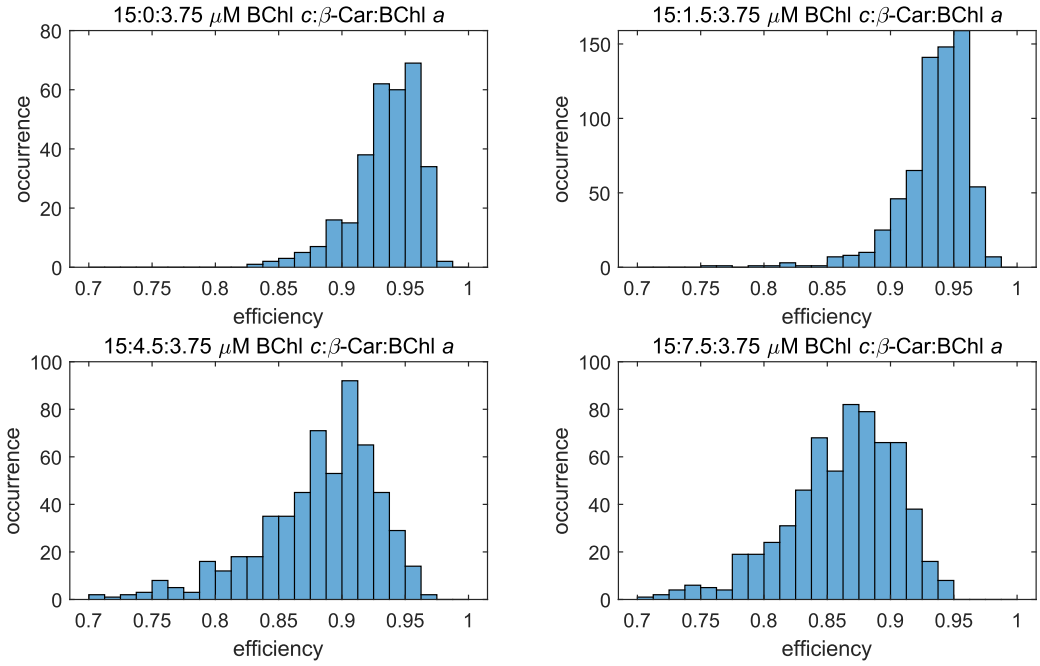

Figure S5: histogram of efficiencies of EET from BChl *c* to BChl *a* when 1% of the brightest detection events are selected.

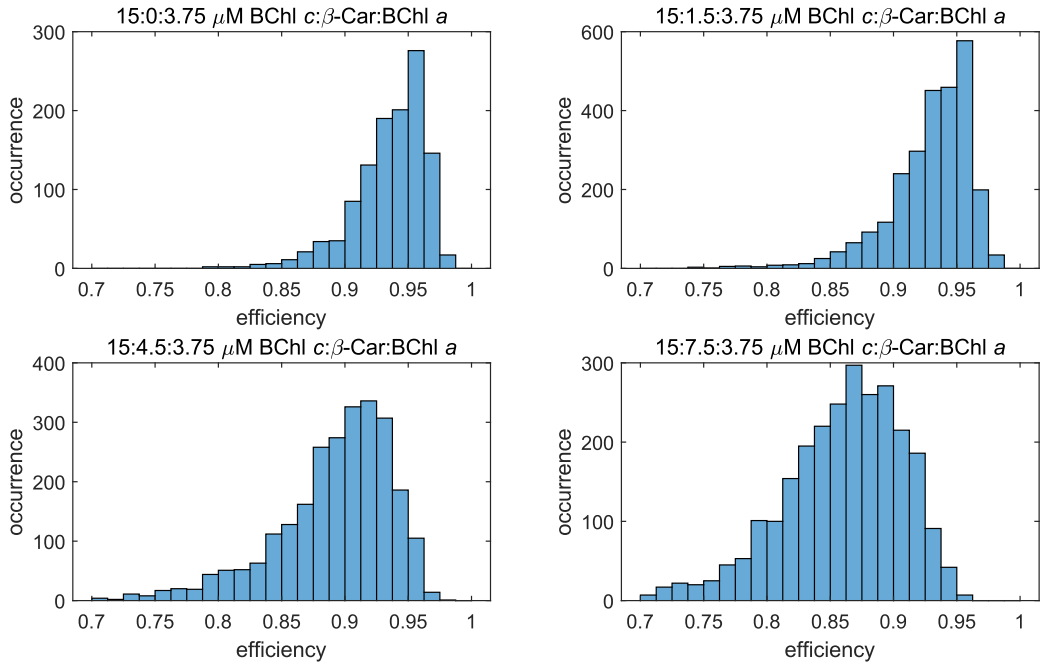

Figure S6: histogram of efficiencies of EET from BChl *c* to BChl *a* when 5% of the brightest detection events are selected.

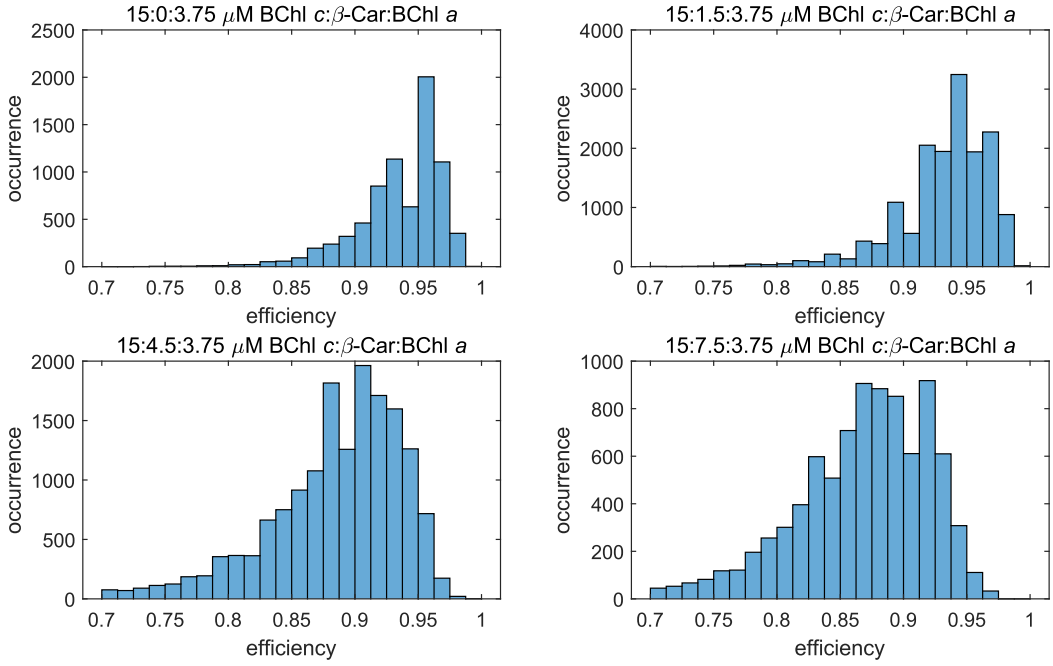

Figure S7[2]: histogram of efficiencies of EET from BChl *c* to BChl *a* when 25% of the brightest detection events are selected.

[2] Due to shot noise, the actual percentages of the brightest detections cross-referenced are 11.5%, 17.9%, 24.5%, and 7.5% in the BChl a channel and 17.1%, 23.3%, 15.2%, and 16.9% in the BChl c channel.

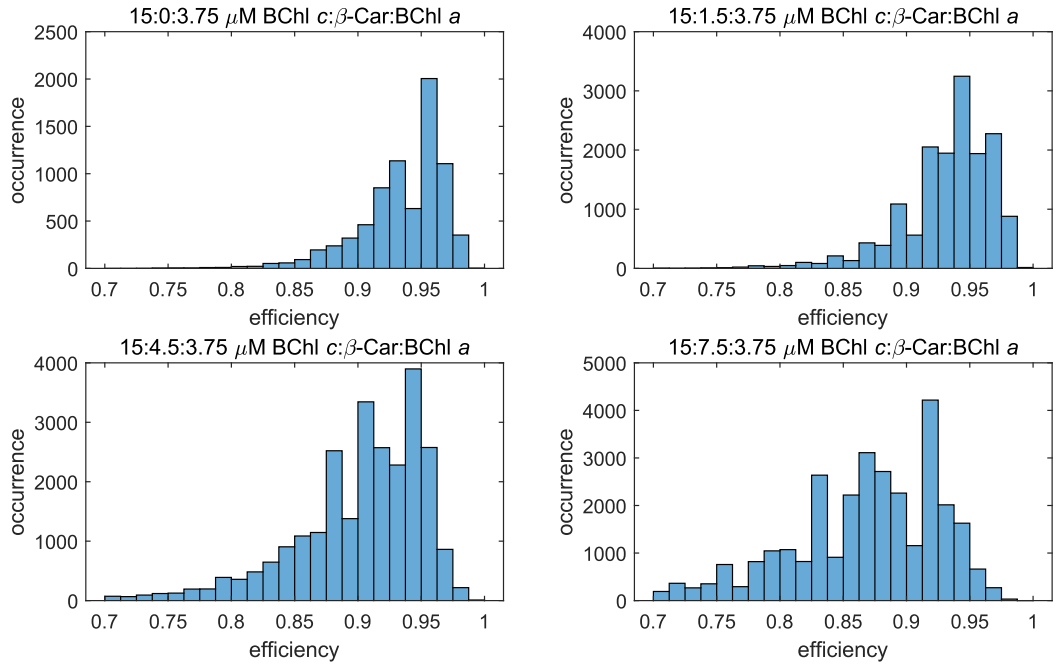

Figure S8[3]: histogram of efficiencies of EET from BChl *c* to BChl *a* when 50% of the brightest detection events are selected.

In total, for liquid samples with 0, 1.5, 4.5 and 7.5 μM beta-carotene, 2028, 6132, 9873 and 11589 particles were analysed using the chosen Poisson threshold, respectively.

For immobilized samples with 0, 1.5, 4.5 and 7.5 μM beta-carotene, 936, 1424, 1866 and 197 particles were detected. It should be noted that the total number of photons detected from the analysed particles of the 7.5 μM β-carotene sample was higher than for the 0 μM beta-carotene sample, and the detected particles with 7.5 μM β-carotene were on average almost 5 times brighter than those without it completely. This was determined to be due to surface quenching being much more pronounced in samples without β-carotene.

[3] Due to shot noise, the actual percentages of the brightest detections cross-referenced are 11.5%, 17.9%, 24.5%, and 26.8% in the BChl a channel and 17.1%, 23.3%, 28.5%, and 41.6% in the BChl c channel. Those are all the detection events containing 2 or more photons in both channels.

4 Sensitivity correction

In a typical scenario, the sensitivity of the two selected spectral channels will not be identical. If the detection probability (Pd) does not change noticeably within the spectral channels, any fluorophore covering both spectral channels can be used for calibration. Fluorescence of this selected fluorophore then needs to be measured both as a steady-state emission (to record the exact fluorescence spectrum) and using the time-resolved setup (to record sufficient number of particles/counts to obtain a representative ratio of intensity in both detection channels).

Multiplying the measured steady-state fluorescence emission spectrum by the transmittance of used filters for each channel and comparing the intensities of both obtained signals will yield the expected ratio of fluorescence on the time-resolved setup. However, due to spectral dependence of reflectivities and transmittances of other elements in the beam path as well as wavelength-dependent sensitivity of the used detectors, this expected ratio will likely differ from the observed ratio. Comparing the expected and observed ratios yields a correction factor by which the signal needs to be corrected in one of the channels. Then, independent efficiencies of EET can be obtained from the measurements.

However, if the Pd changes dramatically within one or both of the channels, using any fluorophore for calibration is no longer possible, because the spectral shape of this fluorophore's emission will not match the emission of the sample. In this presented case of a fluorophore (Fig. S9, left), the expected ratio of acceptor vs donor channel is 0.198, while the measured ratio (not corrected for Pd) is 0.0743, meaning the 840-nm channel is 2.66 times less sensitive. However, using the sample spectrum (Fig. S9, right), we get the expected ratio of 5.14 and the measured ratio of 1.64, resulting in the 840-nm channel being 3.13 times less sensitive. This strong sensitivity dependence on detection wavelength would cause an error in the calculation.

Two solutions for this problem are possible. First, we can measure the full Pd spectral dependence and re-measure it whenever we swap any element in the beam path or adjust the beam alignment. This also requires the Pd to be measured accurately enough with high enough spectral resolution, which was not possible for us. However, a second solution is to use the fluorescence of the sample itself for calibration, as this will account for the spectral shape with respect to the changing Pd, and this approach is much simpler.

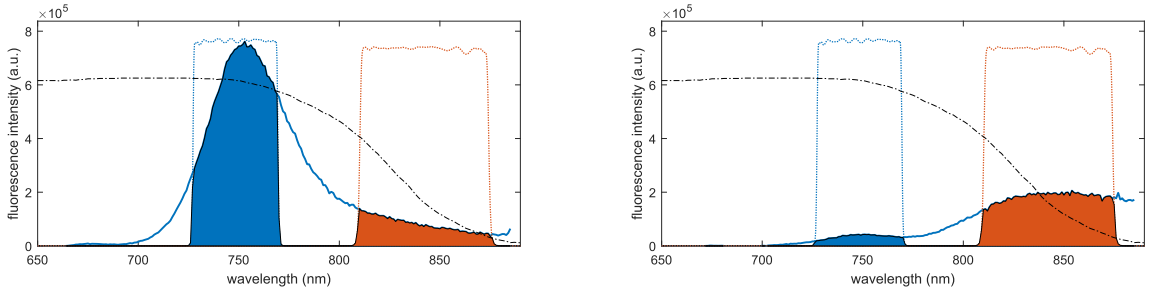

Figure S9: An illustration of a probable Pd curve for fluorescence detection – at the red to NIR limit, the sensitivity of many detection setups (ours included) drops rapidly. This causes photons arriving at the opposite sides of the 840-nm detection channel to be counted with very different probabilities, ultimately invalidating the calibration done by an arbitrary fluorophore.

This is possible because the bulk steady-state emission spectrum is in essence the sum of all the fluorescence recorded from many single particles. This means that the same intensities in the selected detection channels must be recorded if the averaging is done in the bulk sample (many particles emitting at once) or over many individual single particles (many particles emitting and detected consecutively). Therefore, such a calibration by the bulk spectrum of the measured sample normalizes the mean detected efficiency to the bulk value and allows for the photons to be counted correctly. This calibration was used for our data, and the specific calculated values were 7.94, 8.47, 7.86, and 6.78 for samples with 0, 1.5, 4.5 and 7.5 μM β-carotene, respectively. Therefore, the signal obtained in the 840-nm channel was multiplied by these factors for each sample. The minor differences in the factors are caused primarily by changes in the emission spectra across samples with varying β-carotene concentrations – this phenomenon was observed in [2].

For immobilized samples, due to surface-induced quenching, the fluorescence intensity recorded in the 840-nm channel was significantly lower than for the floating samples. This resulted in a much steeper sensitivity correction – values 37.88, 20.90, 26.10, and 19.46 for samples with 0, 1.5, 4.5, and 7.5 μM concentration of β-carotene.

5 *Recorded signal intensities*

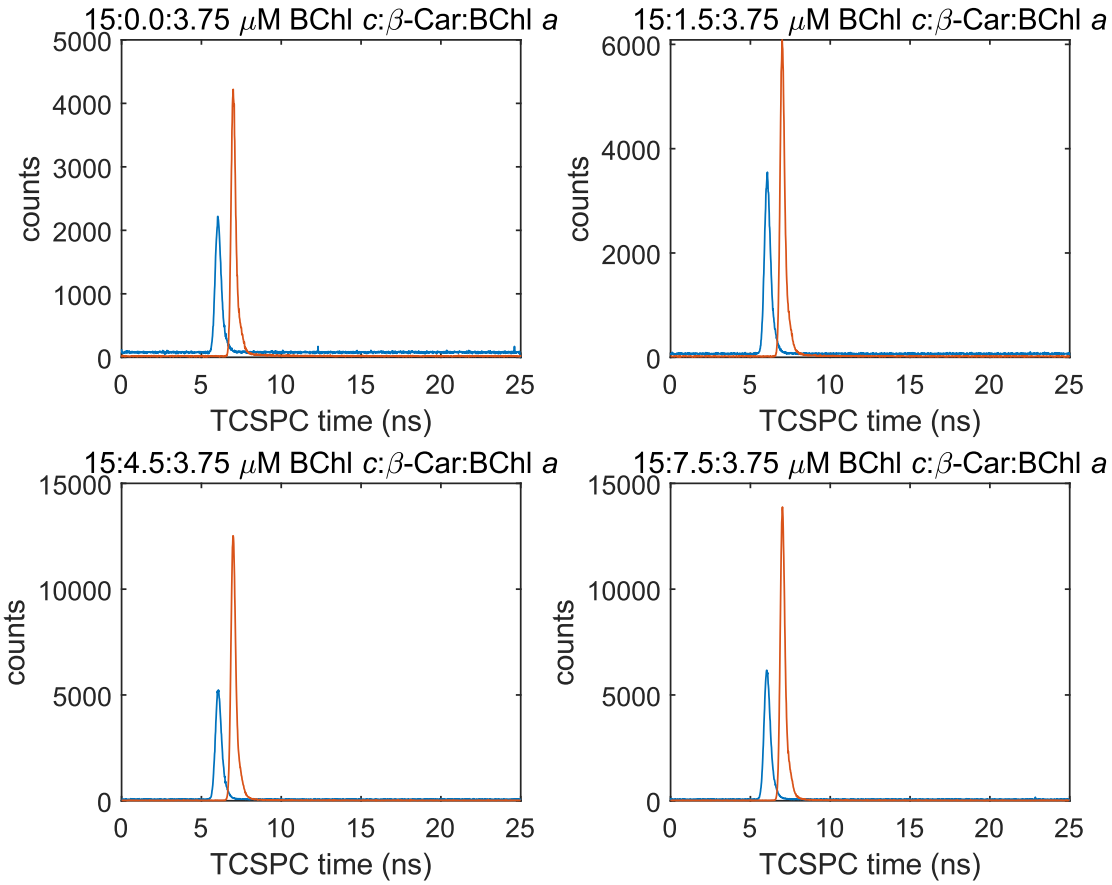

Figure S10: Histograms of photon detection events for one measurement of each sample in liquid phase (floating-particle samples) with different compositions, showing the different number of photons detected from each sample. The median number of detected photons per particle (both channels combined, corrected for background) were 11.7, 13.8, 16.6, and 15.8 for samples with increasing β-carotene concentration. Detections in the 750-nm channel are shown in orange, detections in the 840-nm channel are shown in blue.

6 Size determination by DLS

DLS measurements one day after preparation

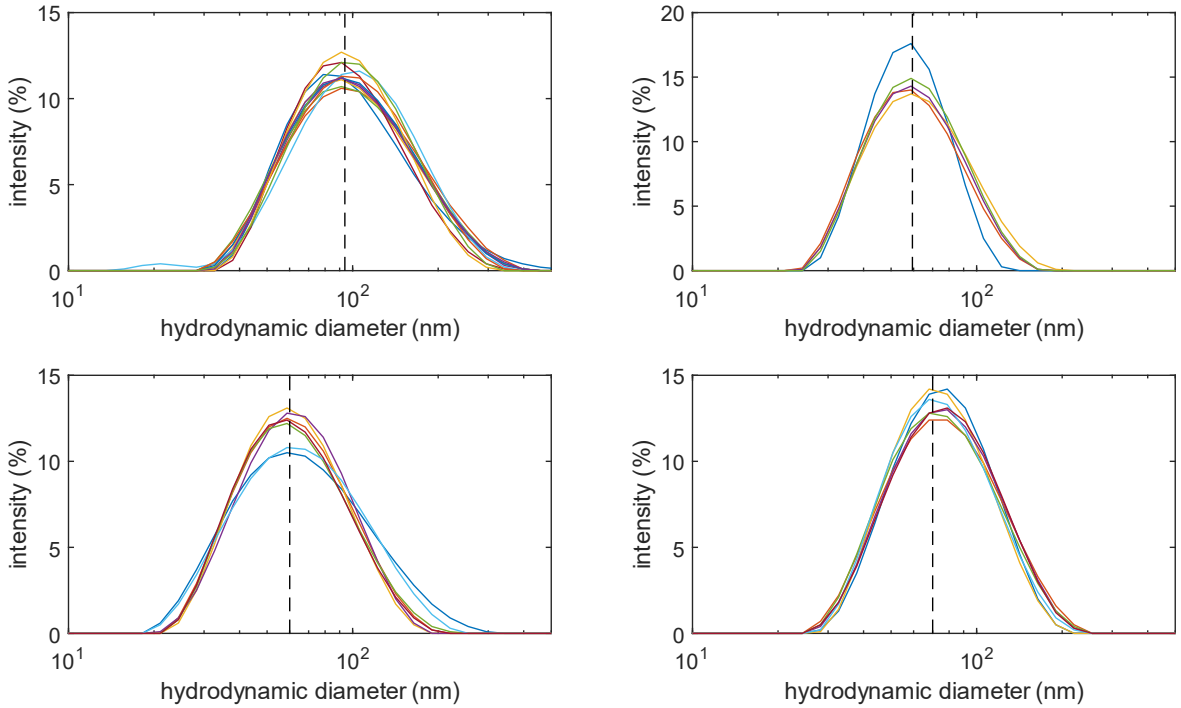

Figure S11: Intensity-weighted distribution of DLS measurements for aggregates without BChl *a* and varying concentrations of β-carotene, top row left to right 0 and 1.5 µM β-carotene, bottom row left to right 4.5 and 7.5 µM β-carotene. The vertical lines show the hydrodynamic diameter (Z-average) for each of the curves. The determined diameter averages for samples with increasing β-carotene concentration are 93.9 nm, 59.4 nm, 60.1 nm, and 70.0 nm. The polydispersity index was 0.22, 0.20, 0.22, and 0.15, respectively. Different colours represent repeated measurements with the same sample.

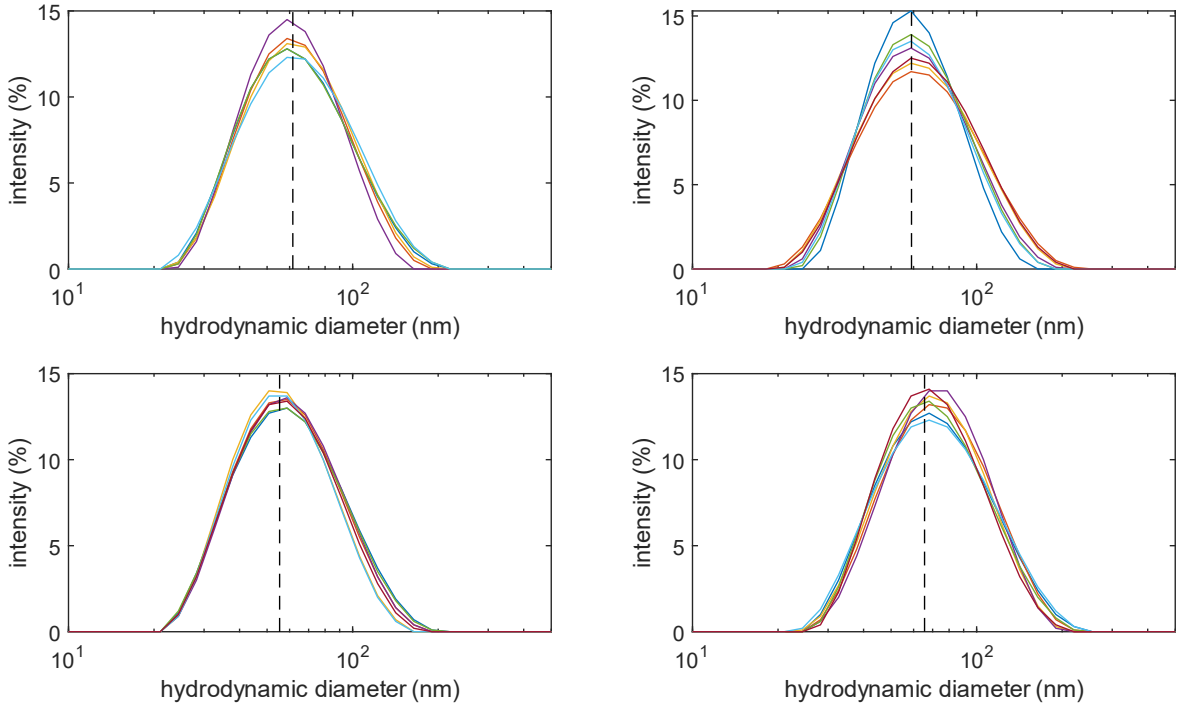

Figure S12: Intensity-weighted distribution of DLS measurements for aggregates with 3.75 µM BChl *a* and varying concentrations of β-carotene, top row left to right 0 and 1.5 µM β-carotene, bottom row left to right 4.5 and 7.5 µM β-carotene. The vertical lines show the hydrodynamic diameter (Z-average) for each of the curves. The determined diameter averages for samples with increasing β-carotene concentration are 61.6 nm, 59.0 nm, 55.3 nm, and 65.6 nm. The polydispersity index was 0.21, 0.19, 0.17, and 0.14, respectively. Different colours represent repeated measurements with the same sample.

DLS measurements two days after preparation

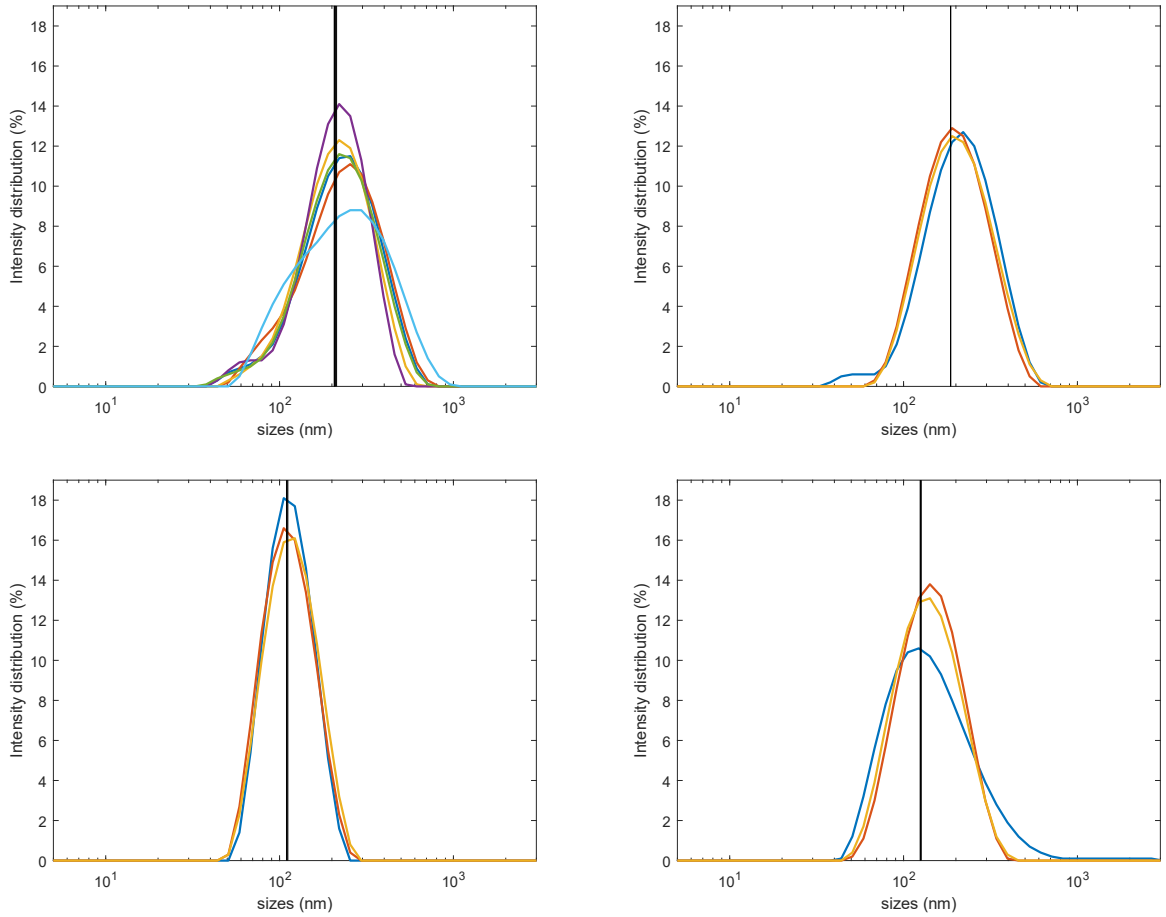

Figure S13: Intensity-weighted distribution of DLS measurements for aggregates without BChl *a* and varying concentrations of β-carotene, top row left to right 0 and 1.5 µM β-carotene, bottom row left to right 4.5 and 7.5 µM β-carotene. The vertical lines show the hydrodynamic diameter (Z-average) for each of the curves. The determined diameter averages for samples with increasing β-carotene concentration are 209, 186, 111, and 125 nm. The dispersity was 0.28, 0.20, 0.13, and 0.17, respectively. Different colours represent repeated measurements with the same sample.

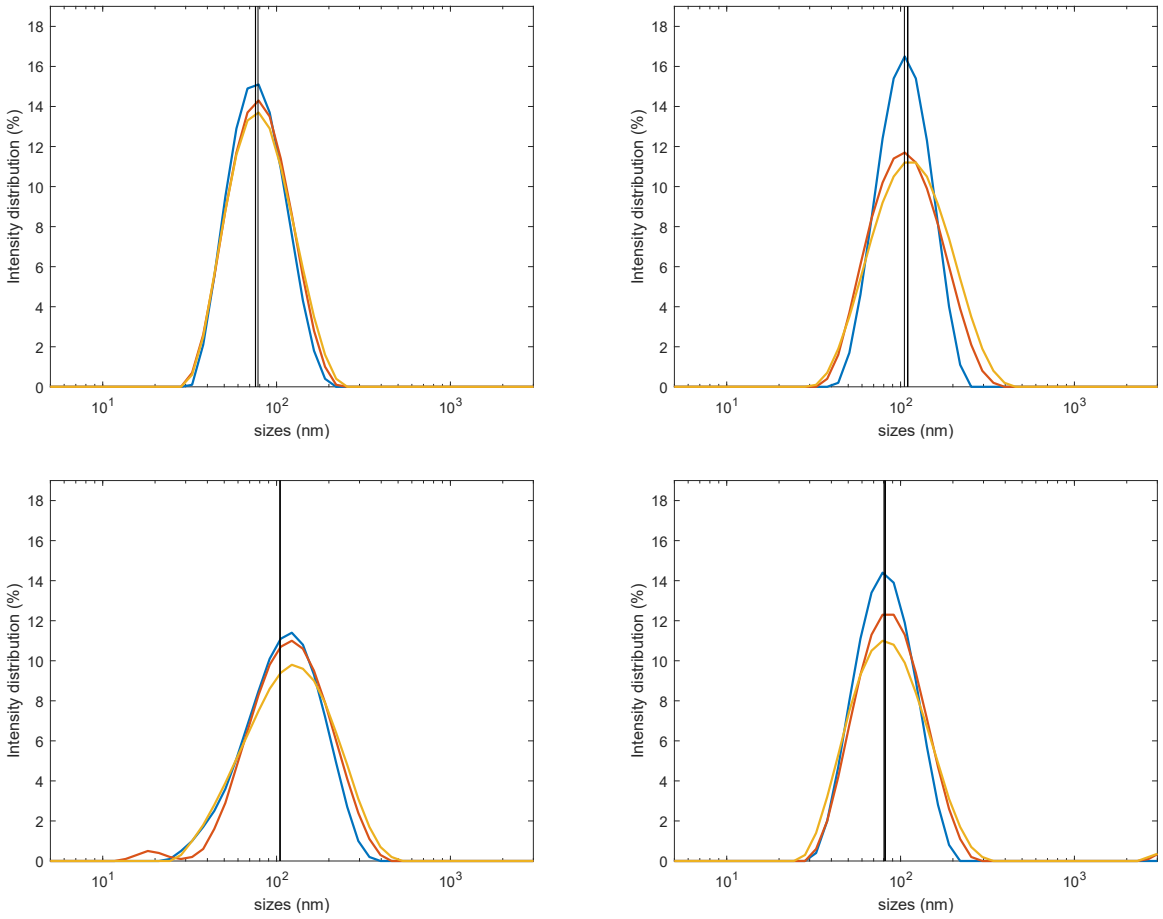

Figure S14: Intensity-weighted distribution of DLS measurements for aggregates with 3.75 µM BChl *a* and varying concentrations of β-carotene, top row left to right 0 and 1.5 µM β-carotene, bottom row left to right 4.5 and 7.5 µM β-carotene. The vertical lines show the hydrodynamic diameter (Z-average) for each of the curves. The determined diameter averages for samples with increasing β-carotene concentration are 77, 108, 105, and 81 nm. The dispersity was 0.17, 0.25, 0.24, and 0.32, respectively. Different colours represent repeated measurements with the same sample.

7 Size determination by FCS

Particle size can also be estimated from FCS. We used FCS to determine whether the sizes of particles we detect are in agreement with sizes determined from DLS measurements. This was done to ensure that we do not detect only a subpopulation of particles for our single-particle experiments, because FCS detects particles based on their luminosity, while DLS should detect all scattering particles in a solution.

We recorded time-tagged time-resolved TCSPC data and performed fluorescence correlation spectroscopy analysis to calculate the autocorrelation function and estimate the residence time of detected particles.

The autocorrelation function (ACF) was fitted as 3D diffusion [3]:

$$G(\tau) = \frac{1}{N\left(1+\frac{\tau}{\tau_D}\right)\sqrt{1+\frac{\tau}{\kappa^2\tau_D}}} + offset \quad \text{(S6)}$$

Where N the number of particles present in the focal volume on average, τ_D is the diffusion (residence) time and κ is the structure parameter of the focal volume which was measured to be 5 (ratio of the longitudinal to transverse axes of the focal volume). The obtained diffusion time was used for further calculations.

The hydrodynamic diameter was then calculated as

$$d_H = \frac{4k_B T\tau_D}{3\pi\eta r^2} \quad \text{(S7)}$$

Where k_B is the Boltzmann constant, T is the thermodynamic temperature, η is the viscosity of the solvent at temperature T (for water at 20°C, this is 1.002 mPa·s), and r is the xy-radius of the focal volume measured to be 145 nm in water.

Table S3: The fitted mean diffusion times and calculated hydrodynamic diameters from FCS and their comparison to values determined from DLS. DLS 1 signifies measurements taken one day after sample preparation, DLS 2 were measurements taken two days after preparation on another replicate of samples. FCS was measured one day after preparation, so it should be compared to column "DLS 1".

	sample	β-carotene concentration	τ_D (ms)	d_H (nm) FCS	d_H (nm) DLS 1	d_H (nm) DLS 2
1	without BChl a	0 µM	3.40	276.7	94	209
5	with BChl a	0 µM	2.56	208.5	62	77
6		1.5 µM	1.84	150.0	59	108
7		4.5 µM	1.99	162.0	55	105
8		7.5 µM	1.80	146.6	66	81

The ACF was fitted with one fast (~ns) and two long (~ms) components which substitute a distribution to a degree (Fig. S15). The short component corresponds to either triplet blinking within the focal volume (triplet states of BChl aggregates have a nanosecond lifetime [4]) or the correlation of detector after-pulsing and is irrelevant to the diffusion analysis. Only the longer millisecond components correspond to the movement of the particles through the volume. Because the measured samples were relatively heterogeneous and polydisperse (Đ around 0.2 or above), using a single long diffusion time was inaccurate. However, a larger number of fitted diffusion times or using a distribution of diffusion times resulted in diverging fits, and therefore two components were used as a compromise.

Samples with higher carotenoid content were generally brighter (samples with 4.5 and 7.5 µM carotenoid concentration vs samples with 0 and 1.5 µM), which aligns with previous results observed in bulk [1, 2]. Here specifically, for floating samples with carotenoid concentration increasing from 0 through 7.5 µM, 2028, 6132, 9873, and 11589 particles respectively were detected from samples of the same pigment concentration. Moreover, measurement duration was longer for samples with low carotenoid content – the FCS was recorded for 40, 30, 20 and 20 minutes, respectively.

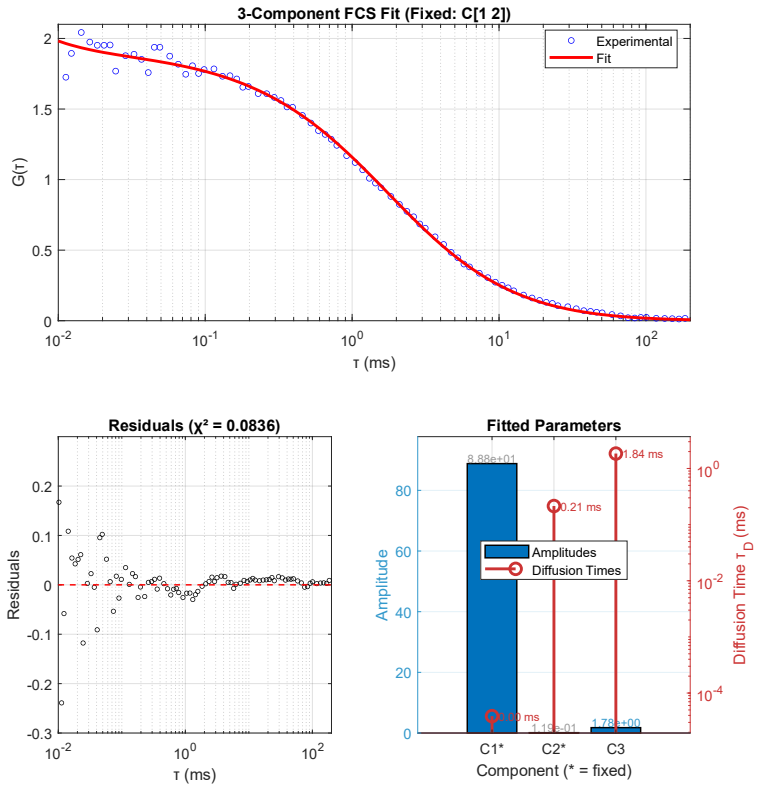

Figure S15: The autocorrelation function and its fit for one of the measurements of sample made of 15 µM BChl *c*, 7.5 µM β-carotene, 3.75 µM BChl *a* with plotted residuals, component amplitudes and diffusion times.

The weighted average of the two long components was used to calculate the diffusion rate and henceforth the hydrodynamic diameter.

From FCS, we determined much larger particles than from DLS measurements. Since DLS is highly sensitive to larger particles (scattering intensity is proportional to d_H^6), it is unlikely that the 2–3 times larger sizes determined from FCS would be bright clusters – those would appear in the DLS measurements and would likely dominate the DLS intensity-weighted size distribution. While analysing the per-particle brightness revealed the median brightness increases with β-carotene content for samples with low β-carotene content, this can be explained as artifacts of the FCS measurement.

The larger sizes determined by FCS can be a result of several effects [5]. The first and foremost is temperature – diffusion is strongly dependent on temperature and even few degrees difference can cause tens of percent error in the determined diffusion coefficient. While DLS measurements were performed in a thermostatically controlled cell, FCS measurements were done under ambient conditions of an air-conditioned laboratory, and the temperature of the sample was not directly controlled. Another factor is the effect of laser fluence. While saturation-free conditions were ensured by the measured power dependence, FCS correlation times are strongly dependent on excitation intensity even at saturation-free intensities [6] . Other factors like coverslip thickness variation or refractive index mismatch of the sample vs de-ionized water also contribute to "blurring" of the focal volume and both are dependent on the depth in sample from which signal is detected [7]. Even a small deviation in these parameters can cause the focal volume to increase significantly if detected deeper into the sample, resulting in particle size overestimation [8, 9].

To explain why the FCS-determined size for the sample without β-carotene is larger than the samples with β-carotene (~280 nm vs ~150 nm), we investigated the mean number of detected photons per particle. Particles in this sample exhibit a smaller median intensity (11.7 photons) compared to other samples (13.8-16.6 photons) (Figure S16a in SI), which is an indication that in this sample without β-carotene, the dimmest (and potentially smallest) particles were not detected by FCS. This sample also has the lowest number of detected photons per particle, (~500 particles per 10-minute measurement vs up to 5000 particles per 10-minute measurement for samples with high β-carotene content). The median particle brightness stays approximately constant for the two samples with the most β-carotene (Figure 16c-d in SI), which indicates that these samples are affected roughly equally, if at all.

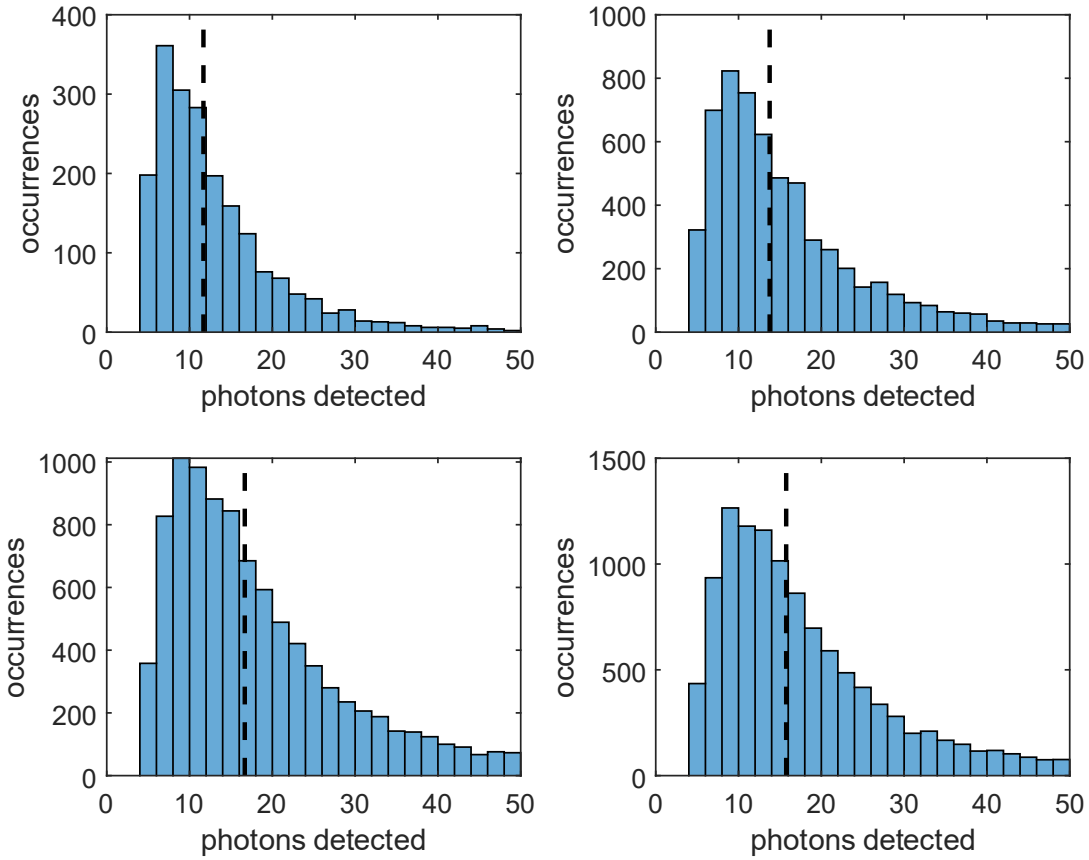

Figure S16: Histograms of the number of photons detected for each analysed particle (sum of both 750-nm and 840-nm spectral channels) in free-floating samples for (a-d) with β-carotene content of 0, 1.5, 4.5, and 7.5 µM, respectively. The samples contained also 15 µM BChl *c* and 3.75 µM BChl *a*. The dashed vertical line indicates the median intensity of the detected particles, corresponding to 11.7, 13.8, 16.7, and 15.8 photons, respectively.

8 FLIM scans

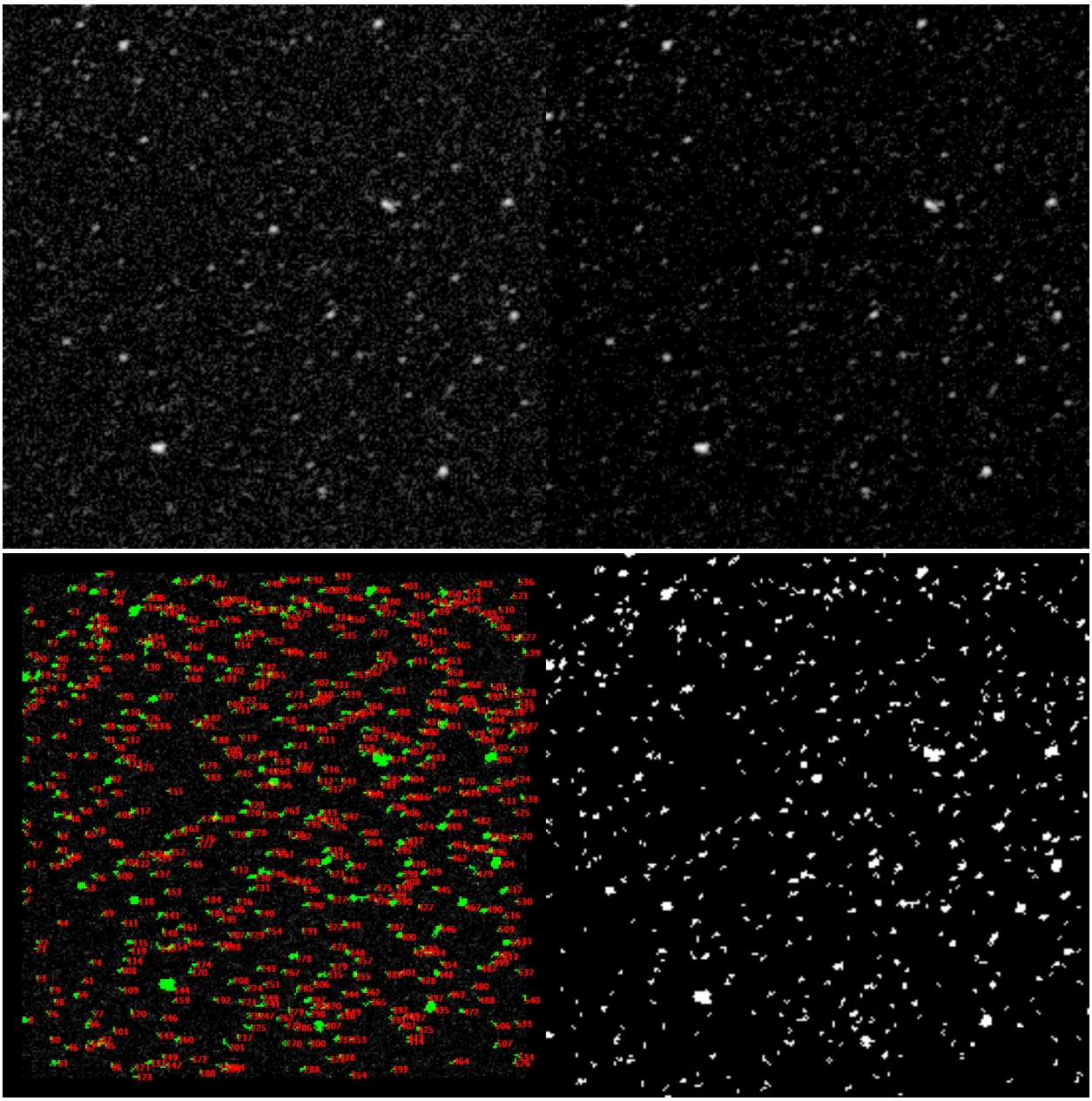

Figure S17: Recorded and processed FLIM scan of sample containing 15 µM BChl *c*, 1.5 µM β-carotene, and 3.75 µM BChl *a* in the 770-nm channel. Top left: original FLIM scan with a logarithmic brightness scale to visualize noise better. Top right: noise-corrected image with a logarithmic brightness scale. Bottom left: original FLIM scan with highlighted and numbered particles, linear brightness scale, overexposed. Bottom right: binary mask of detected particles. The brightest pixel in this scan is 172 photons.

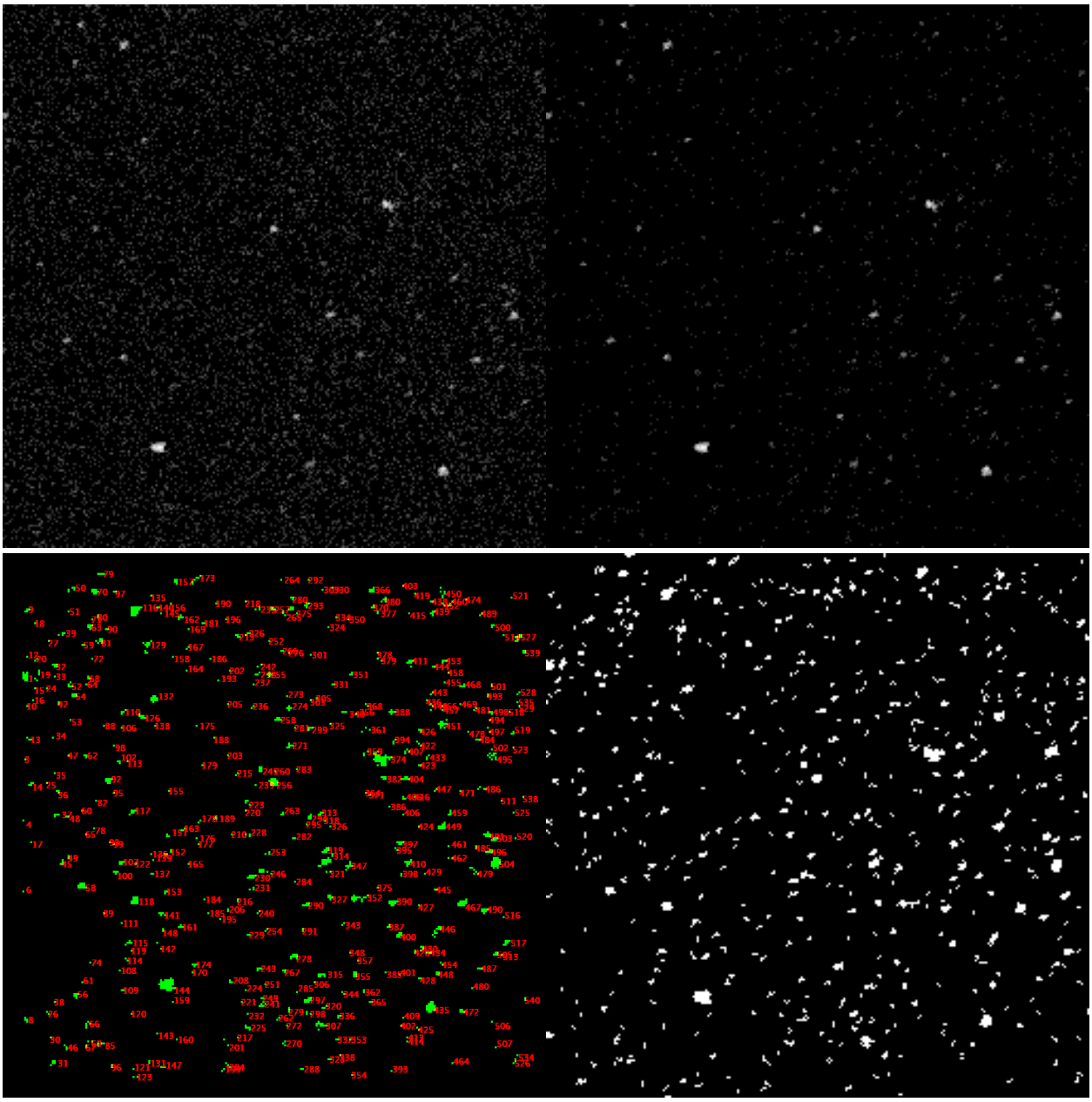

Figure S18: Recorded and processed FLIM scan of sample containing 15 µM BChl *c*, 1.5 µM β-carotene, and 3.75 µM BChl *a* in the 850-nm channel. Top left: original FLIM scan with a logarithmic brightness scale to visualize noise better. Top right: original FLIM scan overlaid with the binary mask made from the 770-nm scan (Fig. S17 bottom right). Bottom left: original FLIM scan with highlighted and numbered particles, linear brightness scale, overexposed. Bottom right: binary mask of detected particles used for the overlay (same as Fig. S17 bottom right). The brightest pixel in this scan is 44 photons.

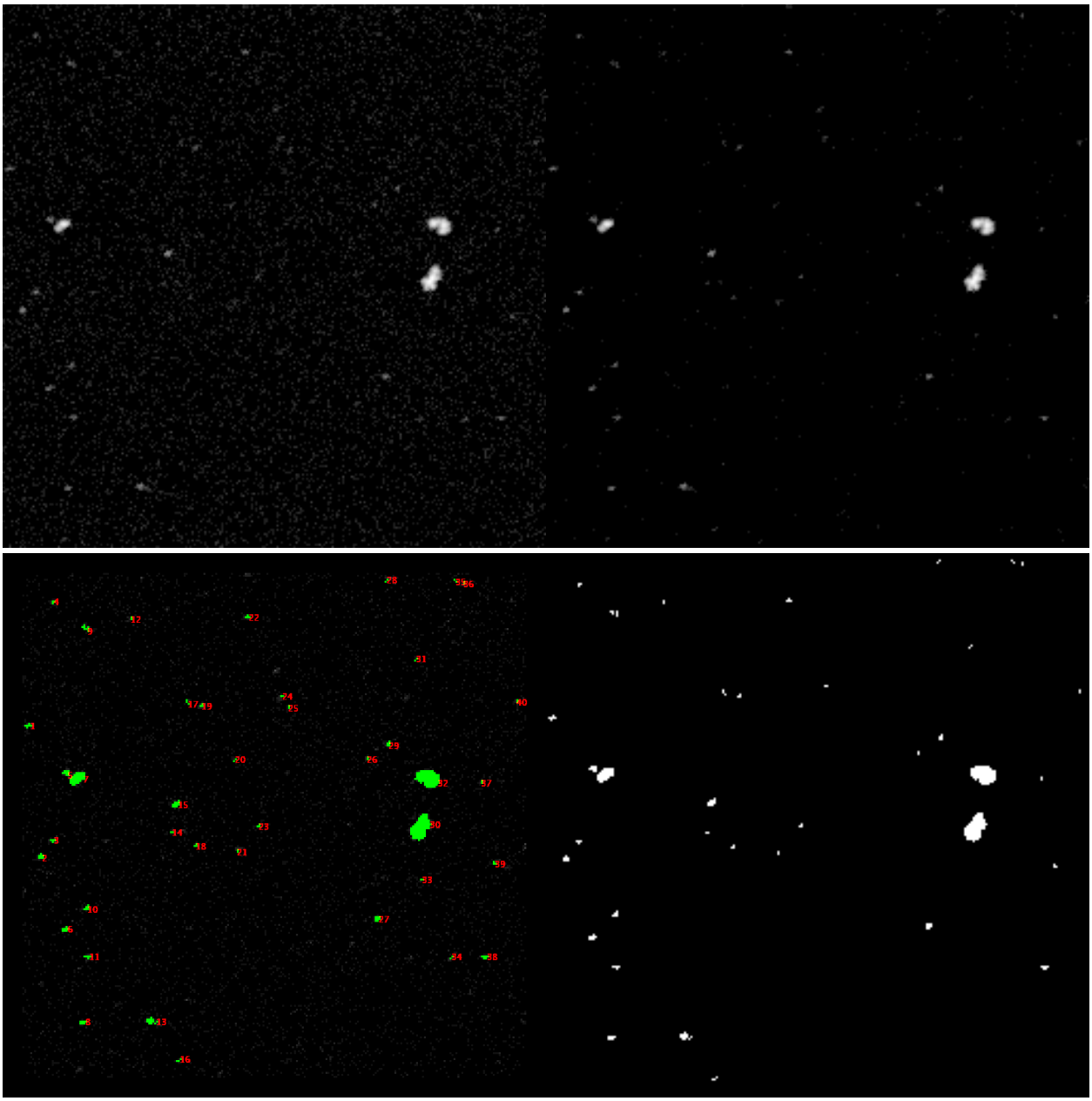

Figure S19: Recorded and processed FLIM scan of sample containing 15 µM BChl *c*, 7.5 µM β-carotene, and 3.75 µM BChl *a* in the 770-nm channel. Top left: original FLIM scan with a logarithmic brightness scale to visualize noise better. Top right: noise-corrected image with a logarithmic brightness scale. Bottom left: original FLIM scan with highlighted and numbered particles, linear brightness scale, overexposed. Bottom right: binary mask of detected particles. The brightest pixel in this scan is 237 photons.

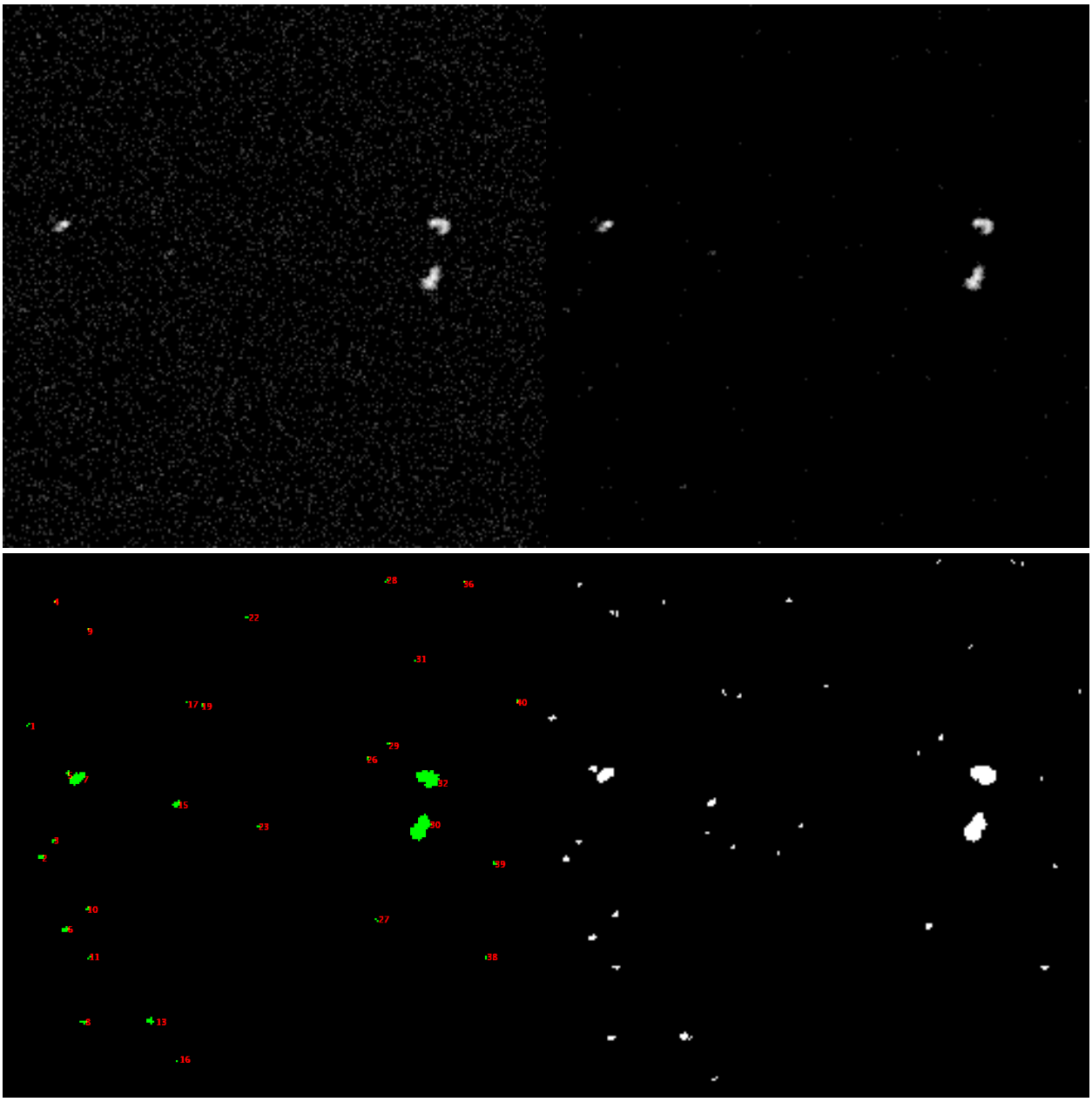

Figure S20: Recorded and processed FLIM scan of sample containing 15 µM BChl *c*, 7.5 µM β-carotene, and 3.75 µM BChl *a* in the 850-nm channel. Top left: original FLIM scan with a logarithmic brightness scale to visualize noise better. Top right: original FLIM scan overlaid with the binary mask made from the 770-nm scan (Fig. S19 bottom right). Bottom left: original FLIM scan with highlighted and numbered particles, linear brightness scale, overexposed. Bottom right: binary mask of detected particles used for the overlay (same as Fig. S19 bottom right). The brightest pixel in this scan is 46 photons.

The observed surface quenching is a result of electron transfer and trapping from the fluorophore to the surface [10, 11]. This is more pronounced on hydrophilized surfaces than on hydrophobic ones [12], and although PLL used in our case likely reduced the effects of surface-induced quenching, it did not prevent it. Intentional electron transfer could be

utilized for depositing artificial antennas onto electrodes in solar or photoelectrochemical cells, for example.

9 *Additional AFM images*

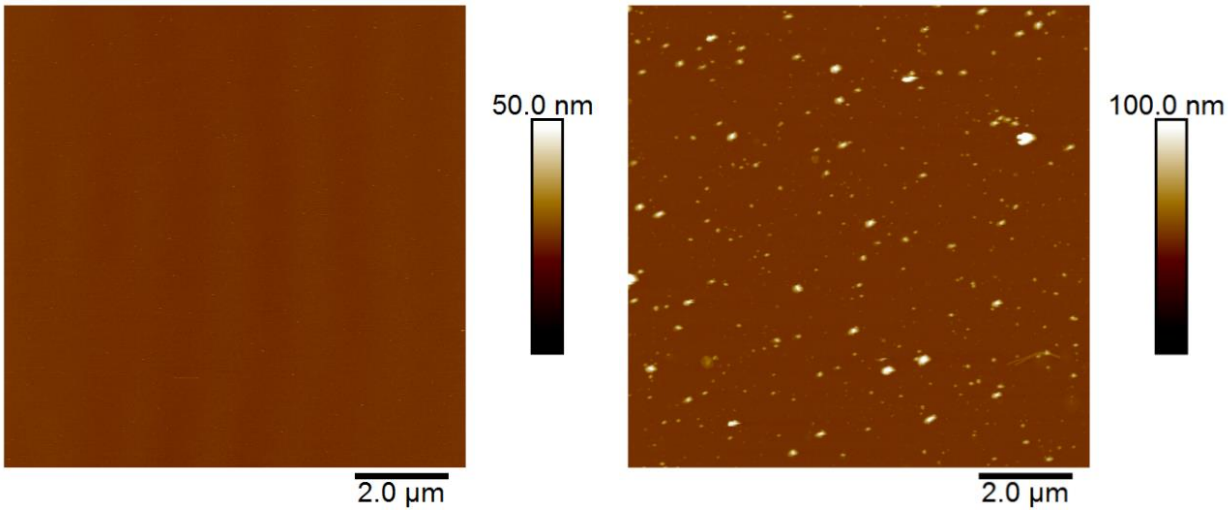

Figure S21: left: PLL-coated glass, right: BChl aggregates deposited on PLL-coated glass

A selection of AFM scans for different tested samples of BChl *c* aggregates with varying concentrations of β-carotene and BChl *a*. The contrast is adjusted so that individual aggregates forming the scanned clusters are better visible, but due to this, the colour axis limits are no longer necessarily represented in the images. This means that the highest point of the first image is not 74.2 nm.

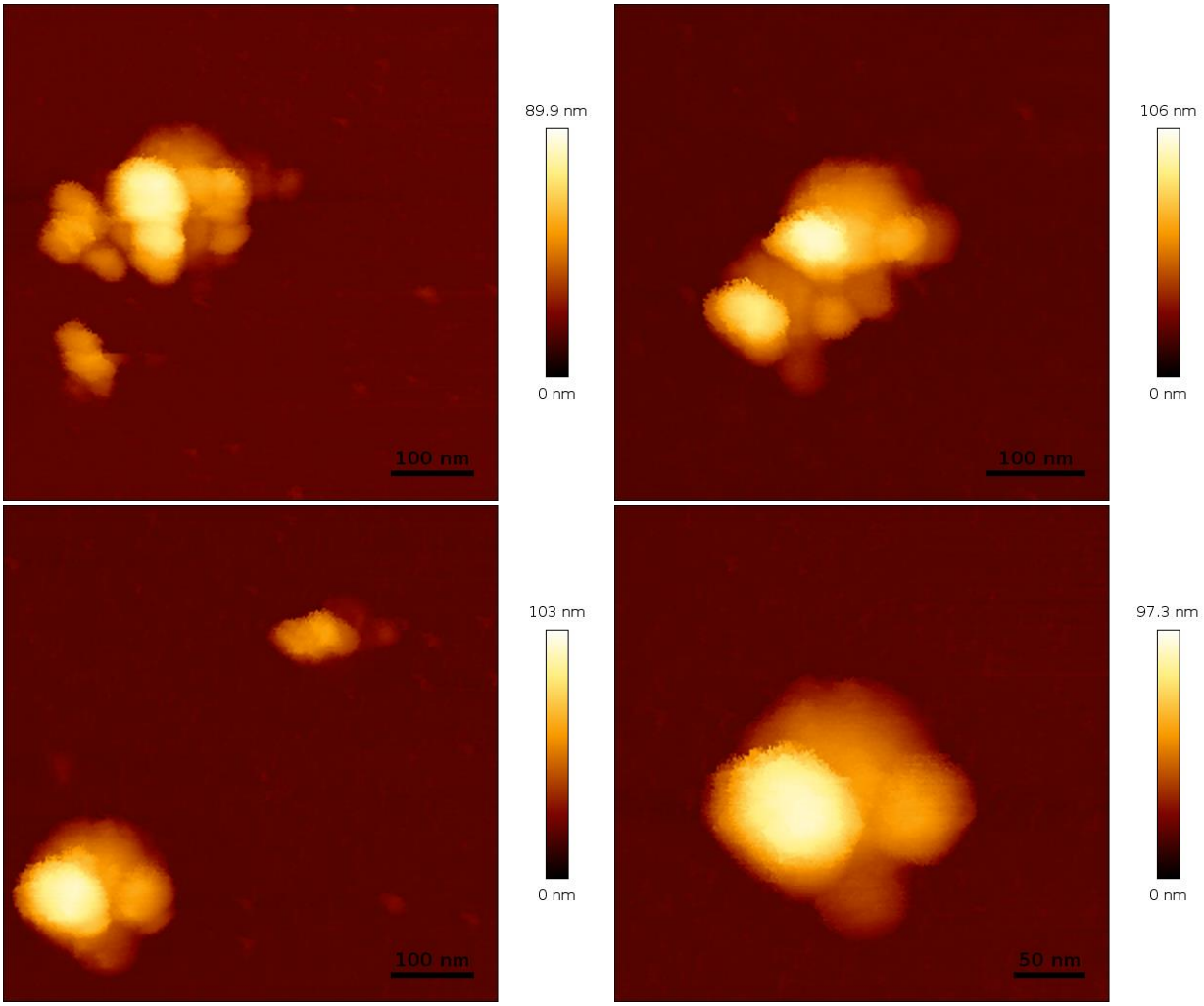

Figure S22: AFM scans of immobilized aggregates prepared as 15 µM BChl *c*, 0 µM β-carotene, and 0 µM BChl *a*.

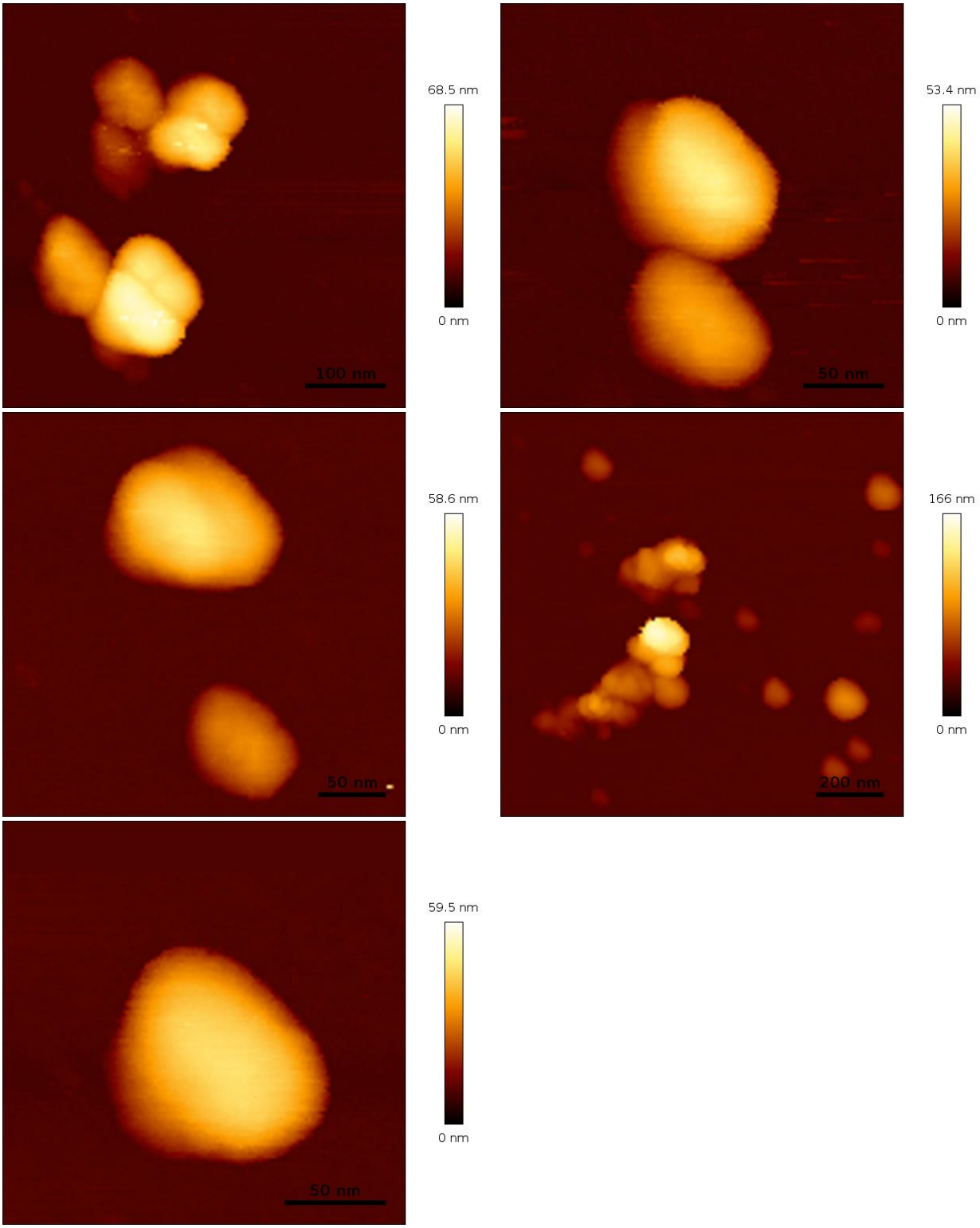

Figure S23: AFM scans of immobilized aggregates prepared as 15 µM BChl *c*, 1.5 µM β-carotene, and 0 µM BChl *a*.

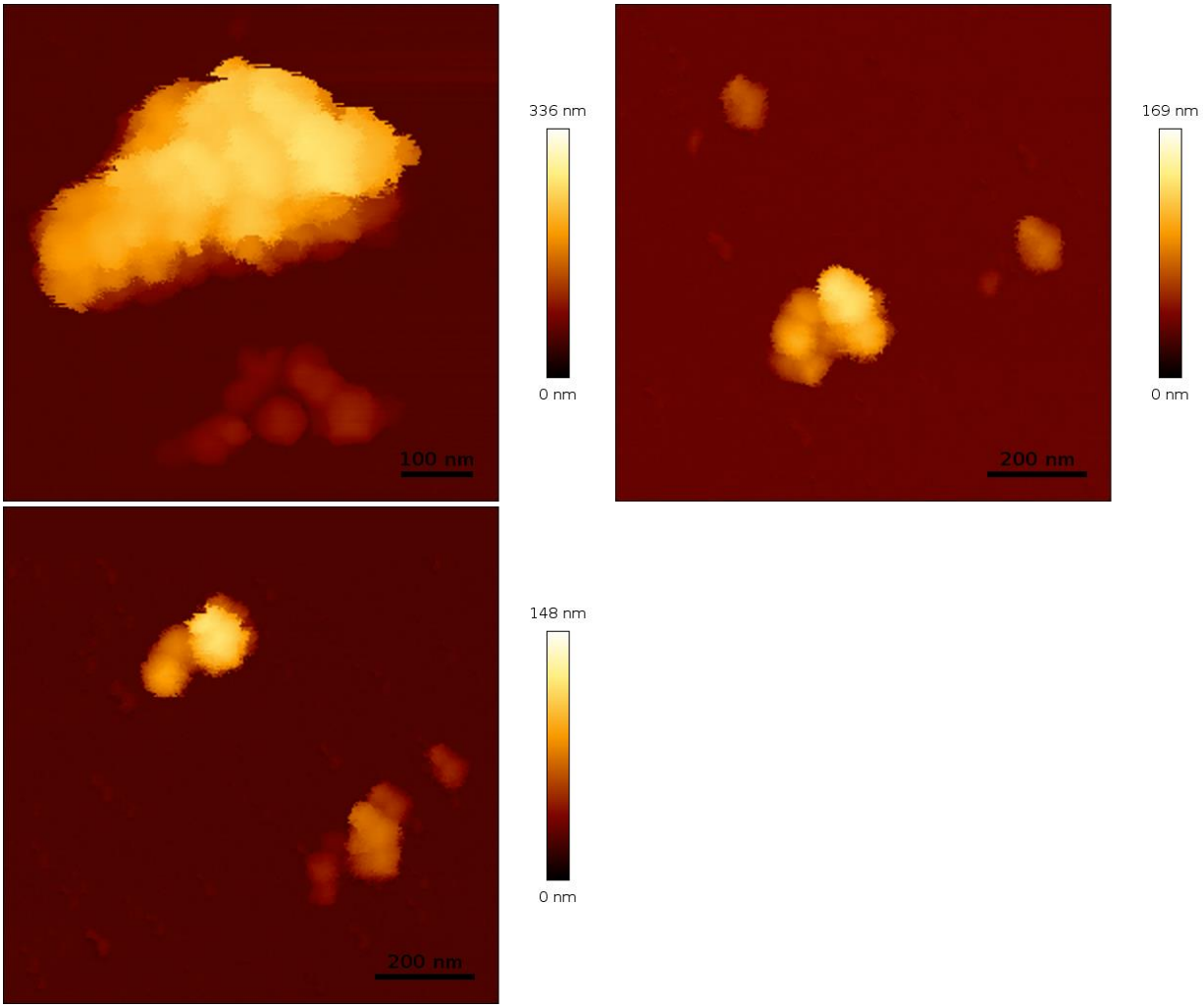

Figure S24: AFM scans of immobilized aggregates prepared as 15 µM BChl *c*, 4.5 µM β-carotene, and 0 µM BChl *a*.

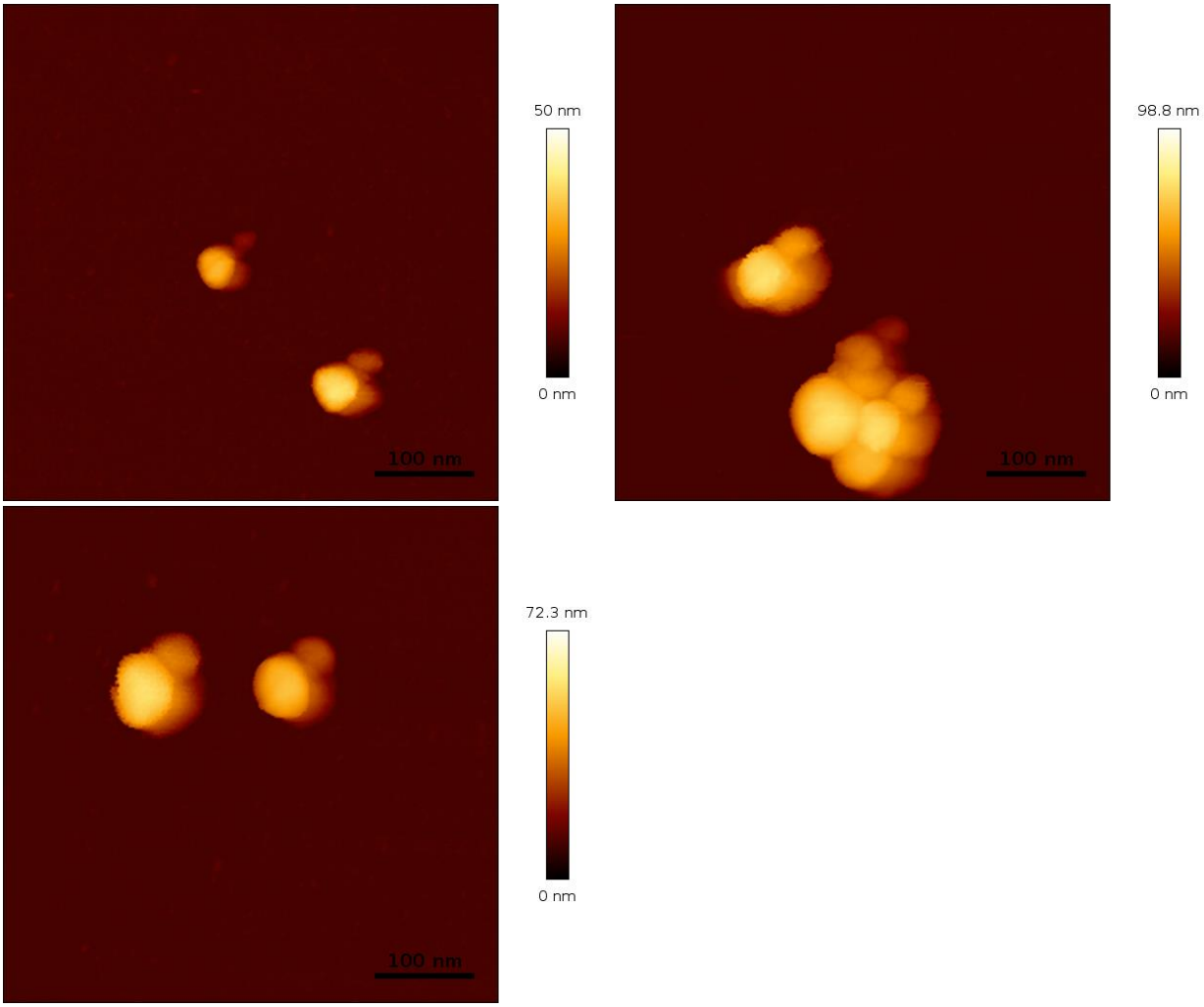

Figure S25: AFM scans of immobilized aggregates prepared as 15 µM BChl *c*, 0 µM β-carotene, and 3.75 µM BChl *a*.

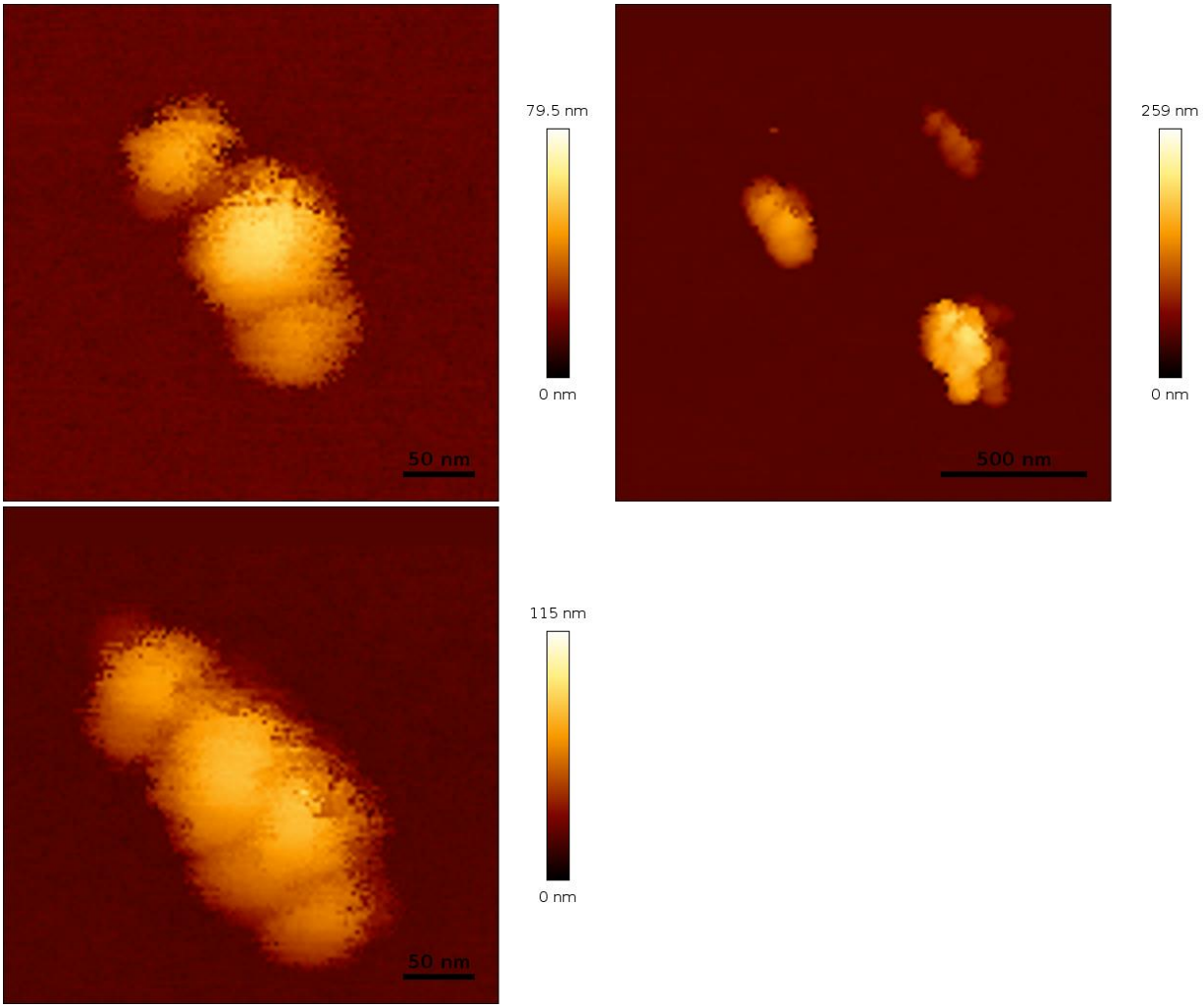

Figure S26: AFM scans of immobilized aggregates prepared as 15 μM BChl *c*, 4.5 μM β-carotene, and 3.75 μM BChl *a*.

10 Power dependence measurements

Before measuring single-particle data, signal power dependence was measured to ensure that aggregates are not saturated by the excitation and annihilation within the aggregates is minimized. Thus, for floating samples, 2.34 µW intensity was used as the highest excitation intensity where saturation and annihilation effects are not yet pronounced while providing the best signal. The signal intensity dependence on excitation power was linear up to at least 2.34 µW.

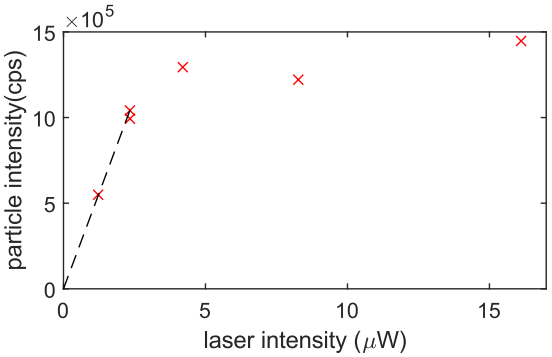

Figure S27: The total fluorescence intensity recorded from particles (aggregates of 15 µM BChl *c*, 1.5 µM β-carotene, and 0 µM BChl *a* as measured in the BChl *c* channel) measured across multiple excitation laser powers. The lowest intensities retain a linear response (dashed line), indicating no saturation, annihilation or photo-damage takes place. At higher excitation intensities, fluorescence stops increasing linearly, as these effects become more pronounced.

References

1. Malina, T., Koehorst, R., Bína, D., Psencík, J. & van Amerongen, H. Superradiance of bacteriochlorophyll aggregates in chlorosomes of green photosynthetic bacteria. *Sci. Rep.* **11**, 8354 (2021).
2. Malina, T., Bina, D., Collins, A.M., Alster, J. & Pšenčík, J. Efficient two step excitation energy transfer in artificial light harvesting antenna based on bacteriochlorophyll aggregates. *J. Photochem. Photobiol. B* **254**, 112891 (2024).
3. Magde, D., Elson, E.L. & Webb, W.W. Fluorescence Correlation Spectroscopy .2. Experimental Realization. *Biopolymers* **13**, 29-61 (1974).
4. Vinklarek, I.S. et al. Triplet state quenching of bacteriochlorophyll c aggregates in a protein-free environment of a chlorosome interior. *Chem. Phys.* **529**, 1110542 (2020).
5. Enderlein, J., Gregor, I., Patra, D., Dertinger, T. & Kaupp, U.B. Performance of fluorescence correlation spectroscopy for measuring diffusion and concentration. *Chemphyschem* **6**, 2324-2336 (2005).
6. Gregor, I., Patra, D. & Enderlein, J. Optical saturation in fluorescence correlation spectroscopy under continuous-wave and pulsed excitation. *Chemphyschem* **6**, 164-170 (2005).
7. Enderlein, J., I, G., Patra, D. & Fitter, J. Art and artefacts of fluorescence correlation spectroscopy. *Curr Pharm Biotechno* **5**, 155-161 (2004).
8. Wan, D.S., Rajadhyaksha, M. & Webb, R.H. Analysis of spherical aberration of a water immersion objective: application to specimens with refractive indices 1.33-1.40. *J Microsc-Oxford* **197**, 274-284 (2000).
9. Mahajan, V.N. Strehl Ratio for Primary Aberrations in Terms of Their Aberration Variance. *J Opt Soc Am* **73**, 860-861 (1983).
10. Liang, Y. & Goncalves, A.M.P. Time-Resolved Measurements of the Fluorescence of Rhodamine-B on Semiconductor and Glass Surfaces. *J. Phys. Chem.* **89**, 3290-3294 (1985).
11. Lee, M., Kim, J., Tang, J. & Hochstrasser, R.M. Fluorescence quenching and lifetime distributions of single molecules on glass surfaces. *Chem. Phys. Lett.* **359**, 412-419 (2002).
12. Quiroz-Segoviano, R.I.Y. et al. On Tuning the Fluorescence Emission of Porphyrin Free Bases Bonded to the Pore Walls of Organo-Modified Silica. *Molecules* **19**, 2261-2285 (2014).